

REPORT DOCUMENTATION PAGE				Form Approved OMB No. 0704-0188	
Public reporting burden for this collection of information is estimated to average 1 hour per response, including the time for reviewing instructions, searching existing data sources, gathering and maintaining the data needed, and completing and reviewing this collection of information. Send comments regarding this burden estimate or any other aspect of this collection of information, including suggestions for reducing this burden to Department of Defense, Washington Headquarters Services, Directorate for Information Operations and Reports (0704-0188), 1215 Jefferson Davis Highway, Suite 1204, Arlington, VA 22202-4302. Respondents should be aware that notwithstanding any other provision of law, no person shall be subject to any penalty for failing to comply with a collection of information if it does not display a currently valid OMB control number. PLEASE DO NOT RETURN YOUR FORM TO THE ABOVE ADDRESS.					
1. REPORT DATE (DD-MM-YYYY) 05-09-2014		2. REPORT TYPE		3. DATES COVERED (From - To)	
4. TITLE AND SUBTITLE Pitching Flexible Propulsors: Experimental Assessment of Performance Characteristics				5a. CONTRACT NUMBER	
				5b. GRANT NUMBER	
				5c. PROGRAM ELEMENT NUMBER	
6. AUTHOR(S) Egan, Brendan Christopher				5d. PROJECT NUMBER	
				5e. TASK NUMBER	
				5f. WORK UNIT NUMBER	
7. PERFORMING ORGANIZATION NAME(S) AND ADDRESS(ES)				8. PERFORMING ORGANIZATION REPORT NUMBER	
9. SPONSORING / MONITORING AGENCY NAME(S) AND ADDRESS(ES) U.S. Naval Academy Annapolis, MD 21402				10. SPONSOR/MONITOR'S ACRONYM(S)	
				11. SPONSOR/MONITOR'S REPORT NUMBER(S) Trident Scholar Report no. 425 (2014)	
12. DISTRIBUTION / AVAILABILITY STATEMENT This document has been approved for public release; its distribution is UNLIMITED.					
13. SUPPLEMENTARY NOTES					
14. ABSTRACT Many applications for Autonomous Underwater Vehicles (AUV) require higher maneuverability than is available with traditional propulsion. An understanding of flexible propulsor performance characteristics is required for application in marine systems. This project investigates relationships between a flexible propulsors' instantaneous shape, performance, and interaction with the surrounding fluid. The analysis is conducted through reduction of the measured force and torque data and multiple wake flow analysis techniques, including particle image velocimetry and dye injection. The experiments take place in USNA's large water channel, using full span flexible propulsor models. The propulsor pitches about a fixed axis at its quarter chord, with a six-axis load cell measuring the forces and torques on the shaft. The non-dimensional parameters, the Reynolds Number, Strouhal Number, and Stiffness Constant, act as a reference for the efficiency of the propulsor and the Coefficients of Thrust and Lift. The ensemble data will facilitate the engineering of fish-like propulsion systems for future application of this technology.					
15. SUBJECT TERMS biological fluid dynamics, hydroelasticity, propulsion, swimming, flexible propulsor					
16. SECURITY CLASSIFICATION OF:			17. LIMITATION OF ABSTRACT	18. NUMBER OF PAGES 58	19a. NAME OF RESPONSIBLE PERSON
a. REPORT	b. ABSTRACT	c. THIS PAGE			19b. TELEPHONE NUMBER (include area code)

U.S.N.A. --- Trident Scholar project report; no. 425 (2014)

**PITCHING FLEXIBLE PROPULSORS: EXPERIMENTAL ASSESSMENT OF
PERFORMANCE CHARACTERISTICS**

by

Midshipman 1/C Brendan C. Egan
United States Naval Academy
Annapolis, Maryland

Certification of Advisers Approval

Associate Professor Mark M. Murray
Mechanical Engineering Department

Associate Professor Cody J. Brownell
Mechanical Engineering Department

Acceptance for the Trident Scholar Committee

Professor Maria J. Schroeder
Associate Director of Midshipman Research

USNA-1531-2

Abstract

Inspiration from nature can provide insight for some of the most longstanding engineering challenges. When comparing marine propulsion systems, traditional propellers and rudders lack the acceleration and maneuverability provided by the organic movement of fish. The fish's unsteady dynamics make it a relatively intricate system, but a reduced order system may reveal the most important dynamic mechanisms. Using a flexible hydrodynamic foil that pitches to produce thrust, the most pertinent aspects of a fish-like propulsion system may be replicated in an engineering environment. The pitching and flexing combination creates a hydroelastic coupling in which the fluid and flexible foil simultaneously affect each other's behavior.

An understanding of flexible propulsor performance characteristics is required for application in marine systems. Although the system can be modeled in computer simulations, these may disregard several significant factors. Thus, the experimental campaign seeks to more fully explain the influence of the fluid-structure coupling and viscous effects on performance.

The project investigates relationships between the propulsors' instantaneous shape, performance, and interaction with the surrounding fluid. The analysis is conducted through reduction of the measured force and torque data and multiple wake flow analysis techniques, including particle image velocimetry and dye injection. The experiments take place in USNA's large water channel, using full span flexible propulsor models. The propulsor pitches about a fixed axis at its quarter chord, with a six-axis load cell measuring the forces and torques on the shaft. The non-dimensional parameters, the Reynolds Number, Strouhal Number, and Stiffness Constant, act as a reference for the efficiency of the propulsor and the Coefficients of Thrust and Lift. The ensemble data will facilitate the engineering of fish-like propulsion systems for future application of this technology.

Keywords: biological fluid dynamics, hydroelasticity, propulsion, swimming, flexible propulsor

Acknowledgements

Don Bunker
John Zselezcky
Dan Rhodes
Louise Becnel
Fritz Woolford

Prof. Joel Schubbe
ENS Michael McPherson
Tom Price
Brandon Stanley
Bill Beaver

Mike Superczynski
Timothy Snipes
David Majerowicz
Joe Dillard
Daniel Rodgerson

Table of Contents

ABSTRACT.....	1
ACKNOWLEDGEMENTS	1
TABLE OF CONTENTS.....	2
LIST OF FIGURES	3
NOMENCLATURE	6
BACKGROUND	6
RESEARCH SUMMARY	9
EXPERIMENTAL DETAILS	9
EXPERIMENTAL SETUP.....	11
A. TEST SECTION	11
B. GROUNDING BOARD.....	12
C. FLEXIBLE FOIL	12
<i>Material Testing and Results</i>	14
D. LOAD CELL	18
E. MOTOR.....	19
F. MOUNTING APPARATUS	20
1. Motor Mounting Plate.....	20
2. Motor Collar.....	22
3. Foil Bracket	24
4. Isolation Pucks.....	25
PARAMETER SPACE.....	26
LOAD CELL ANALYSIS AND RESULTS.....	27
PARTICLE IMAGE VELOCIMETRY ANALYSIS AND RESULTS	41
DYE INJECTION ANALYSIS AND RESULTS	51
CONCLUSIONS.....	54
FUTURE WORK.....	56
RESEARCH CONTRIBUTIONS	57
REFERENCES	58

List of Figures

Figure 1: PilotFish prototype demonstrates the capabilities of using flexible propulsors for highly maneuverable vehicles.	7
Figure 2: (a) Carangiform type fish propulsion system (Murray, 1999) and (b) rigid oscillating foil (Schnipper, 2009).	8
Figure 3: Propulsor efficiencies for various Stiffness Constants and dimensionless frequencies for (a) the rigid heaving propulsor (Murray, 1999) and (b) the flexible flat plate propulsor (Dai, 2012).	8
Figure 4: General schematic of the pitching flexible propulsor in the USNA water channel.	11
Figure 5: Water channel at the USNA Hydrodynamics Laboratory with transparent walls to allow analysis of the flow.	12
Figure 6: The grounding board of water channel prevents free-surface interaction during the tests.	12
Figure 7: Approximate shape of flexible propulsor used in the experiments.	13
Figure 8: Open mold with aluminum backbone to produce geometrically identical propulsors with a rigid front quarter.	13
Figure 9: Completed flexible propulsor inside the open mold after curing.	14
Figure 10: Flex 40 "dog bone" material testing specimens before tensile testing.	15
Figure 11: Flex 40 material specimen undergoing tensile testing at approximately 200% and 400% strain.	15
Figure 12: Flex 40 "dog bones" after material testing show breaks at bubbles present in the material.	16
Figure 13: Load-displacement plot from the tensile test for the Flex 40 Alumilite material.	16
Figure 14: Stress strain diagram of Flex 40 material with linear regression to calculate the modulus of elasticity.	17
Figure 15: Load cell used to measure forces and torques on the shaft with amplifier box and connecting cable.	18
Figure 16: Motor for manipulating the angular position of the foil and controller box.	19
Figure 17: Drawing of the testing apparatus that was outfitted into the water channel.	20
Figure 18: Drawing of the motor mounting plate, which secures the motor to the water channel.	21
Figure 19: Testing apparatus without motor in place showing the motor collar extending through the mounting plate.	21
Figure 20: Motor apparatus propped up by 2" square bars accounting for height of the isolation pucks on the load cell.	22
Figure 21: The motor collar attaches to the motor shaft and transmits torque to the rest of the testing apparatus.	22
Figure 22: Motor collar attached to motor next to mounting plate.	23
Figure 23: Amended collar design to allow utilization of the motor shaft's interior threading. ...	23
Figure 24: Drawing of the foil bracket that serves as a transition from the load cell to the foil. .	24

Figure 25: Both sides of the foil bracket showing the adjustable bolts holding the aluminum backbone in place.....	25
Figure 26: Isolation puck and transparent view of hole pattern with 45° offset to electrically isolate the load cell.....	25
Figure 27: Isolation pucks attached to either side of the load cell to prevent electrical interference.	26
Figure 28: The fully specified parameter space determines the independent variables used in the experiment.....	27
Figure 29: Time domain results for the force in line with the foil for a high efficiency run of the Flex 30 propulsor.	29
Figure 30: Force measured perpendicular to the foil face at a constant flow speed, stiffness, and frequency in separate oscillations.	30
Figure 31: Force measured perpendicular to the foil before and after application of a low pass filter.....	31
Figure 32: Unfiltered and filtered force data in the frequency domain with zeroed values above the cutoff frequency.	32
Figure 33: Unfiltered, filtered, and excessively filtered force data perpendicular to the foil.....	33
Figure 34: Transformed thrust and lift force data correlating to the direction of the flow.....	33
Figure 35: Thrust and lift forces from a lower Strouhal Number run with the Flex 30 foil resulting in -0.1% efficiency.....	35
Figure 36: Calculated Coefficients of Thrust for the ensemble of foils.	35
Figure 37: Shaft torque plotted against the angular position.	36
Figure 38: Shaft torque multiplied by angular velocity plotted against angular position showing different behavior and values for high (left) and low (right) Strouhal Number oscillations.	37
Figure 39: Efficiency for the rigid foil oscillations compared to the predictions from the numerical model (Murray, 1999).....	38
Figure 40: Raw efficiency calculated for the entire parameter space with overlaid spline functions fit to each foil.	39
Figure 41: Three-dimensional plot of Strouhal Number, Stiffness Constant, and efficiency.....	40
Figure 42: Schematic of particle image velocimetry data collection apparatus used to generate a vector field of the flow.....	41
Figure 43: Expected wake vorticity interactions for a negative (top), zero (middle), and positive (bottom) efficiency case with an example from a maximum efficiency case of the Flex 60 foil.	42
Figure 44: Image captured by the PIV system and the same image after preprocessing to remove the mean image.	43
Figure 45: PIV images from each quarter cycle of the Flex 60 foil's maximum efficiency run (red = positive and blue = negative vorticity).	44
Figure 46: Image labeling convention used to reference foil location and direction of motion for all PIV images.....	45

Figure 47: PIV images from each quarter cycle of the Flex 60 Foils zero efficiency run (red = positive and blue = negative vorticity).....	46
Figure 48: PIV images from each quarter cycle of the Flex 60 negative efficiency run (red = positive and blue = negative vorticity).....	47
Figure 49: PIV images from negative efficiency run for Flex 30 (left), Flex 60 (center), and rigid (right) foils (red = positive and blue = negative vorticity).	47
Figure 50: PIV images from each quarter cycle of the rigid foil's maximum efficiency case with negative pitchfork bifurcation (red = positive and blue = negative vorticity).	49
Figure 51: PIV images from each quarter cycle of the Flex 30 foil's maximum efficiency case with positive pitchfork bifurcation (red = positive and blue = negative vorticity).....	50
Figure 52: Dye imaging of the Flex 40 foil during oscillations.....	51
Figure 53: Dye injection images from quarter cycles of the high efficiency case of the Flex 40 foil.	52
Figure 54: Tracking of the vortex location for the suspected case of the pitchfork bifurcation for the maximum efficiency case of the rigid foil.	53
Figure 55: Tracking of the vortex location for the suspected case of the pitchfork bifurcation in the opposite direction for the maximum efficiency case of the rigid foil.	53

Nomenclature

b	– Foil Span
c	– Chord Length
C_{Lm}	– Mean Lift Coefficient
C_{Lrms}	– RMS Lift Coefficient
C_T	– Thrust Coefficient
δP	– Pitot Tube Pressure Differential
E	– Modulus of Elasticity
f	– Oscillation Frequency
F_T	– Thrust Force
F_L	– Lift Force
η	– Efficiency
I	– 2D Moment of Inertia
K	– Stiffness Constant
L	– Swept Length
μ	– Water Viscosity
P_{in}	– Power Out
P_{out}	– Power In
θ	– Angular Position
ρ	– Water Density
Re	– Reynolds Number
S	– Swept Distance
St	– Strouhal Number
τ	– Torque
T	– Oscillation Period
V	– Water Velocity
ω	– Angular Velocity
w	– Foil Width

Background

Biological inspiration has provided new insights to many old problems. Some of the best-known examples of bio-inspired engineering include Velcro, sharkskin swimsuits, and Gecko tape (Mueller, 2008). While most marine vessels use traditional propellers and rudders for propulsion and handling, recent research points to the possibility of developing new capabilities by taking advantage of the unsteady dynamics associated with the organic movement of a fish (Triantafyllou, 2004). Straying away from traditional propulsion and mimicking the motion of a fish may have a significant impact on the current doctrine of underwater propulsion techniques. Propellers have demonstrated their effectiveness at attaining high speeds through the water, but the associated rudders are only useful when there is a significant wash over the surface. At low

speeds, ships can become more difficult to maneuver with this system. A fish, however, using coordinated, organic movement, can effectively turn and accelerate from a standstill to pursue prey or escape from a predator. Natural selection suggests that this means of propulsion is effective in hostile underwater environments. Prototype models, shown in Fig. 1, have already demonstrated the capabilities of this technology in the PilotFish project, which was sponsored by the Office of Naval Research in 1997 (Murray, 1999).

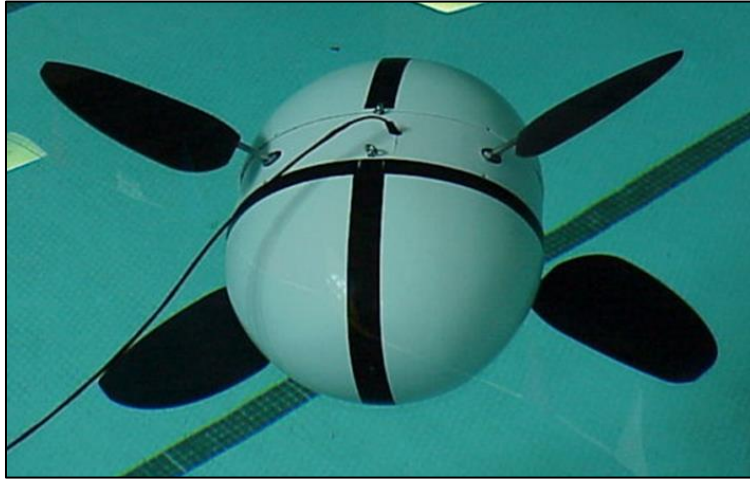


Figure 1: PilotFish prototype demonstrates the capabilities of using flexible propulsors for highly maneuverable vehicles.

The motion of a fish is difficult to artificially reproduce for analysis or for application to marine systems. The complicated dynamics of the unsteady, coupled fluid-structural system make simulation of the interaction between the fish and the environment difficult utilizing traditional computational methods. However, a reduced order system that simplifies the motion down to a few key dynamic mechanisms may be able to produce the same performance as a fish in a way that is easier to mechanize. The most basic designs use a rigid foil pitching about a fixed point. The comparison between the most common type of fish propulsion and the rigid foil design is shown in Fig. 2. Previous analysis of this system shows that by varying the frequency and amplitude of the rigid pitching propulsor, the number and type of vortices shed per oscillation into the wake can vary significantly (Schnipper, 2009). This analysis also shows that the vorticity of the wake directly relates to the amount of thrust, drag, and lift produced while the foil oscillates (Schnipper, 2009).

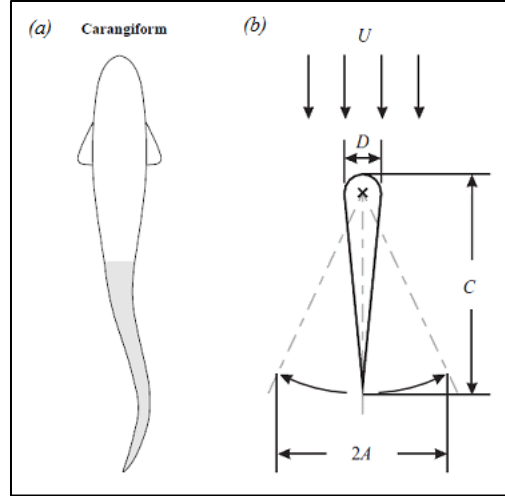


Figure 2: (a) Carangiform type fish propulsion system (Murray, 1999) and (b) rigid oscillating foil (Schnipper, 2009).

The simply pitched foil, however, does not fully represent the organic motion of many underwater life forms. Additional research incorporated a heaving motion in which the foil pitches about a point moving perpendicular to the free-stream flow. To produce optimal thrust, the phase between the pitching and heaving motions must synchronize. This coordination further complicates the propulsor actuation, but the mechanization can be simplified by connecting the pitch point to a spring to allow passive heaving (Murray, 2003). This configuration takes advantage of the natural tendency to heave and allows the variable spring stiffness to contribute to the thrust production and efficiency of the system (Murray, 2003). Additional research investigated a fixed pitch point with a naturally delayed phase heave downstream on a flexible propulsor; however, because of the difficulties of fabrication, the tapered shape is less favorable than a simpler flexible plate of constant thickness. The constant thickness makes the system easier to model and implement, and the flexibility increases the overall efficiency compared to a rigid plate with similar oscillation parameters (Dai, 2012). Efficiency results from models of both the heaving and flexible propulsors are shown in Fig. 3. These graphs indicate that there are points of optimization within the data set that will result in the most efficient performance if the propulsor or spring has the correct pairing of oscillation frequency and stiffness.

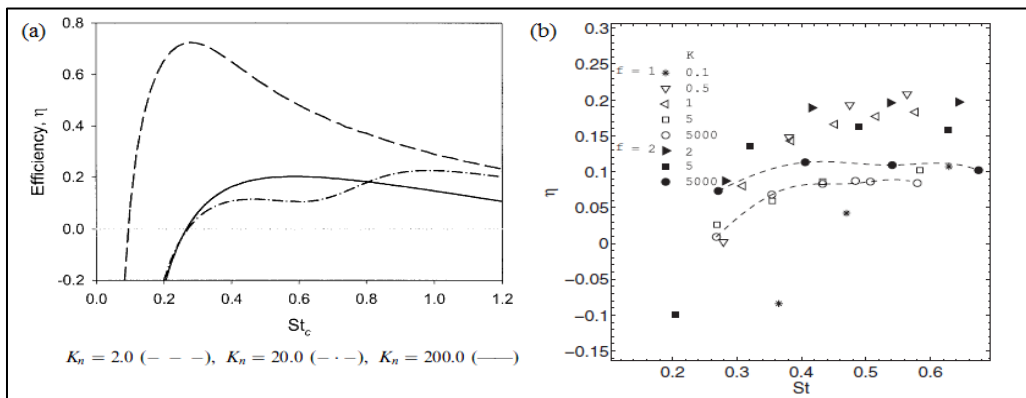


Figure 3: Propulsor efficiencies for various Stiffness Constants and dimensionless frequencies for (a) the rigid heaving propulsor (Murray, 1999) and (b) the flexible flat plate propulsor (Dai, 2012).

While researchers have analyzed both rigid foils and flexible plates, little work has combined flexibility into a foil shape to optimize overall performance. The lack of integration of the hydrodynamic shape and flexible material creates a gap in the current knowledge of the performance of pitching propulsors. Numerical simulations indicate that the flexible foil should have a better overall performance than the flexible plate in both its thrust and efficiency (Murray, 1999). These simulations, however, make several significant assumptions, including the lack of fluid viscosity, that limit their accuracy. Experimental modeling is required to understand the full capabilities of a pitching flexible propulsor while taking into account the effects of viscous drag and boundary layer dynamics (Murray, 1999).

Research Summary

This research project involved experimental testing of the two-dimensional case of a flexible propulsor pitching about a fixed point at its quarter chord. While simplified numerical models have simulated this system before, experimental data are required to verify and update the methods used to calculate the interactions between the foil and the fluid. The tests were conducted in the USNA Hydrodynamics Laboratory water channel using a full span, standard NACA foil. The performance characteristics of thrust and efficiency were analyzed with respect to the foil stiffness, the water channel velocity, and the oscillation frequency. These three independent parameters have the greatest effect on the hydrodynamic interaction between the flexible foil and fluid (Dia, 2012, and Triantafyllou, 2004). Within this interaction, the pitch and flex of the foil affect the fluid behavior while the fluid in turn affects the instantaneous shape and motion of the foil. An analysis of the trends in performance characteristics with respect to the input parameters determined what combinations return the optimal thrust and efficiency. The use of dimensional analysis populated the test matrix with the three independent experimental parameters to be tested. The forces and torques acting on the propulsor were measured throughout the oscillations by a six-axis load cell. Vortex formation and propagation in the wake of the propulsor were examined using particle image velocimetry (PIV). A camera synchronized with dye, which was injected into the flow, captured the qualitative interaction between the fluid and the foil. Ultimately, the project hoped to produce a better understanding of the hydrodynamic coupling between the fluid and the foil and facilitate the application of flexible propulsors to marine vehicles.

Experimental Details

Using dimensional analysis, the relevant non-dimensional parameters were determined for experimental investigation. The dimensionless parameters used for this analysis include the Reynolds Number (Re), Strouhal Number (St), Stiffness Constant (K), and Swept Distance (S),

$$Re = \frac{\rho V c}{\mu}, \quad (1)$$

$$St = \frac{fL}{V}, \quad (2)$$

$$K = \frac{EI}{0.5\rho V^2 c^3}, \quad (3)$$

$$\text{and } S = \frac{L}{c}, \quad (4)$$

where ρ is the fluid density, V is the free-stream velocity, c is the chord length, μ is the fluid viscosity, f is the oscillation frequency, L is the swept length, E is the modulus of elasticity, and I is the 2D moment of inertia. In fluid dynamics, the Reynolds Number (Re) represents the ratio of inertial to viscous forces in the fluid and characterizes the kinematic behavior of the fluid. The Reynolds Number provides insight in determining whether the flow exhibits laminar or turbulent characteristics, which affects the formation of vortices in the wake. The Strouhal Number (St) is used in reference to flow over an oscillating object. It is representative of the extent and frequency of the oscillation relative to the free-stream velocity of the fluid. Previous research has shown that the Strouhal Number has been of most significance for oscillating propulsor performance (Dai, 2012). The Stiffness Constant (K) represents the ratio of forces required to bend the foil to the fluid pressure forces available in the flow. The flexibility and bending of the propulsor determine the amount of fluid-structure coupling in the system. The Swept Distance (S) relates the extent of the pitching motion to the size of the foil traveling through that motion, and it is significant in understanding the magnitude of the oscillation throughout each cycle.

The independent variables in each experiment include the material elasticity, fluid velocity, and oscillation frequency. The elasticity of the material was determined by the various grades of urethane used to make the flexible propulsors. The modulus of elasticity affected only the Stiffness Constant, but only six values were available for the stiffness, dictated by the six materials used for propulsor fabrication. The fluid velocity was controlled by changing the flow rate of the water channel used in the experiment. Because this control affects all three dimensionless parameters, the velocities were chosen with care to ensure a thorough exploration of the parameter space. A motor programmed to oscillate according to a given sinusoidal function controlled the oscillation frequency. The amplitude of the oscillation angle was the same for all experiments, $\pm 15^\circ$.

The following dependent variables were of interest in the experiment: thrust/drag force, lift force, torque required to turn the shaft, instantaneous angular position and velocity, power in, power out, efficiency, and wake flow structure. The instantaneous angular position was recorded as a phase reference for the other collected data. The power into the foil is calculated from the integrated torque and angular velocity, the power out is the integrated thrust/drag force times the flow speed, and the efficiency is the power out divided by the power in. The interaction with the

surrounding fluid was observed using photography synchronized with dye injection. The velocity field in the wake, along with numerous calculated metrics, was measured using PIV.

Experimental Setup

Figure 4 shows a general schematic of the setup for the testing of the pitching flexible propulsor. Within the test section, water flows over a full span foil, which is oscillating according to specified frequencies programmed into the drive motor. The force gages on the shaft between the motor and foil measure the forces and torques acting on the propulsor. The grounding board prevents free-surface interaction to test the 2D flow case, and the free-flood area prevents ventilation of air back into the test section.

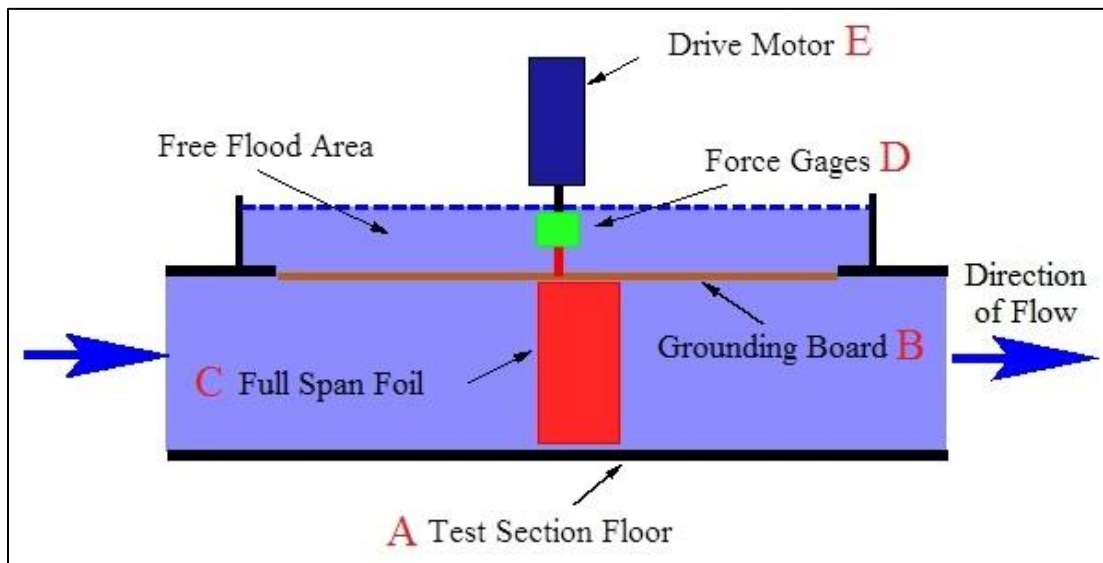


Figure 4: General schematic of the pitching flexible propulsor in the USNA water channel.

A. Test Section

The experiment was conducted in the large water channel of the USNA Hydrodynamics Laboratory. The test section of the channel, shown in Fig. 5, has a 40 cm x 40 cm cross-section along a length of 150 cm, and is capable of flow velocities up to 6 m/s. Three of the four walls of the water channel are transparent to allow observation and analysis of the hydrodynamic interactions between the propulsor and fluid. The density and viscosity of the water varied slightly from one test to the next as the temperature of the water varied with the changing seasons, but the temperature, recorded whenever tests were conducted, never varied more than three degrees throughout the entire experiment. These slight changes were considered negligible, and the standard temperature and pressure values for density and viscosity were used in calculations.



Figure 5: Water channel at the USNA Hydrodynamics Laboratory with transparent walls to allow analysis of the flow.

B. Grounding Board

The opaque grounding board, shown in Fig. 6, creates an upper bound to the water flow to prevent any free-surface interactions with the pitching foil or created vortices. The shaft of the foil extends through the hole seen in the center of the grounding board. The rectangular cutout is removable to allow the foil to be exchanged or adjusted without removing the entire grounding board. The water flows through the water channel cross-section and floods freely over the top of the grounding board to prevent any air from ventilating into the model through the shaft hole.

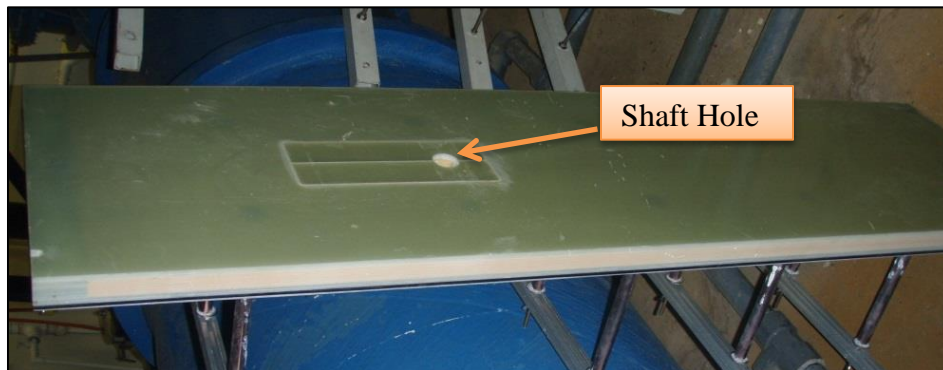


Figure 6: The grounding board of water channel prevents free-surface interaction during the tests.

C. Flexible Foil

The cross-section of the foil was a standard NACA0015 airfoil, as shown in Fig. 7. The series designator, 0015, indicates that the foil was symmetrical with a maximum thickness of 15% of the chord length. The 40 cm height of the foil ensured that the model spans nearly the full height of the test section to minimize the end effects of fluid flowing around the top and bottom of the propulsor, which allowed testing of the near 2D case. Using the same mold for the creation of each foil ensured the width, height, and chord length, as shown in Fig. 7, were held constant throughout the tests.

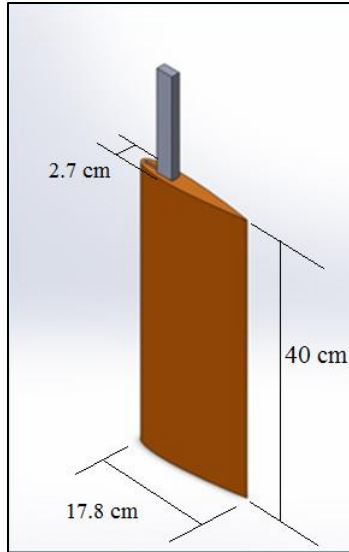


Figure 7: Approximate shape of flexible propulsor used in the experiments.

The foils were made of various grades of Alumilite Flex urethane poured into a cast around an aluminum backbone, shown in Fig. 8. To make the cast, the two halves of the mold fit together with the backbone in place, and the Alumilite was poured into the large hole on the top of the mold. Two holes on either side of the backbone and the pouring hole allowed the gas contained within the mold to escape as the Alumilite was poured, settled, and cured.

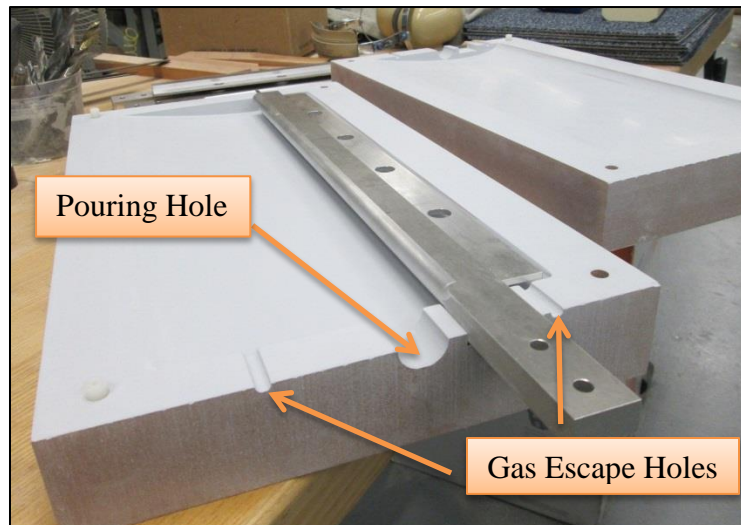


Figure 8: Open mold with aluminum backbone to produce geometrically identical propulsors with a rigid front quarter.

The backbone was designed to stay in place within the foil and have good contact with the urethane cast. The thin portion that extends to the front of the foil ensures that the front quarter of the propulsor is effectively rigid. The extension is thinner than the rest of the backbone so that it can extend almost all the way to the front of the foil without breaking through the curved surface of the leading edge. The four holes along this extension ensure a quality grip between the urethane and backbone. The urethane fills these holes when it is poured into the mold, and

once cured, the urethane in the holes prevents the backbone from slipping out of the molded foil. The trailing edge of the backbone is curved, rather than square, to prevent internal tearing due to the stress concentration in the urethane around the backbone. The two holes on the backbone, shown extending out of the mold in Fig. 8, are in a standard configuration to allow the load cell and motor to attach to the foil. On the bottom end of the backbone is a pin that keeps the backbone centered in the casting while the urethane is being poured. The foil and mold were designed in conjunction with an independent research project conducted by Ensign Michael McPherson, USNA class of 2013.

The finished product of the casting is shown in Fig. 9. The stiffness of the finished foil depends on the grade of the Alumilite used. The elasticity of each grade of urethane was determined utilizing a separate testing specimen cast from the same Alumilite mixture used for foil casting.



Figure 9: Completed flexible propulsor inside the open mold after curing.

Material Testing and Results

To determine the Stiffness Constant of each of the foils, material testing was conducted on standard “dog bones” made out of each of the six materials in the same pour as the foil to ensure near identical composition. The “dog bone” and tensile testing procedure come from ASTM D638 for tensile testing of plastics and D412 for testing of rubber elastomers, respectively. Figure 10 shows the four Flex 40 “dog bones” prior to their material testing. The “dog bones,” like the fins, contain some smaller bubbles throughout, but due to the thin mold for the “dog bones,” they were more prone to large bubbles such as the ones seen in the bottom left corner of Fig. 10. In order to compensate for the reduced area and stress concentration where there were bubbles, the material tests were conducted at a reduced initial gage length for some of the specimens when necessary.

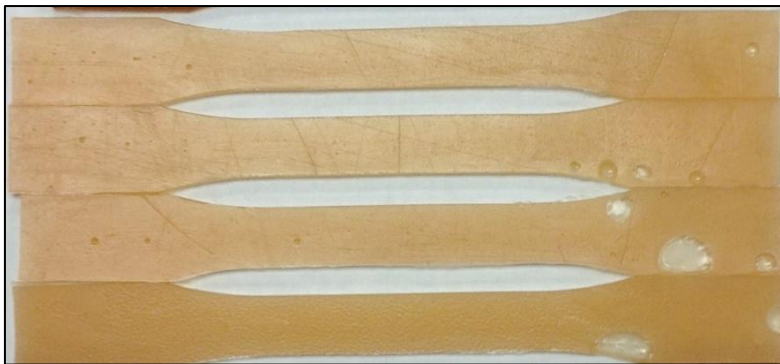


Figure 10: Flex 40 "dog bone" material testing specimens before tensile testing.

The tensile test used a single-axis transducer to measure the tensile force in the material as it was pulled. The apparatus in Fig. 11 is typically used for pulling thin fibers, which makes it ideal for measuring the small forces generated when stretching some of the lower stiffness Flex materials. While some of the specimens were pulled until failure, others continued to stretch until the machine no longer had enough height to pull any further. Specimens that had many small internal bubbles tended to break at lower strains when compared to the specimens that had fewer bubbles. This likely contributed to error in the stiffness measured during the tests, but the error introduced from these small bubbles was not significant enough to cause a large enough error in one material relative to the properties measured of any other.

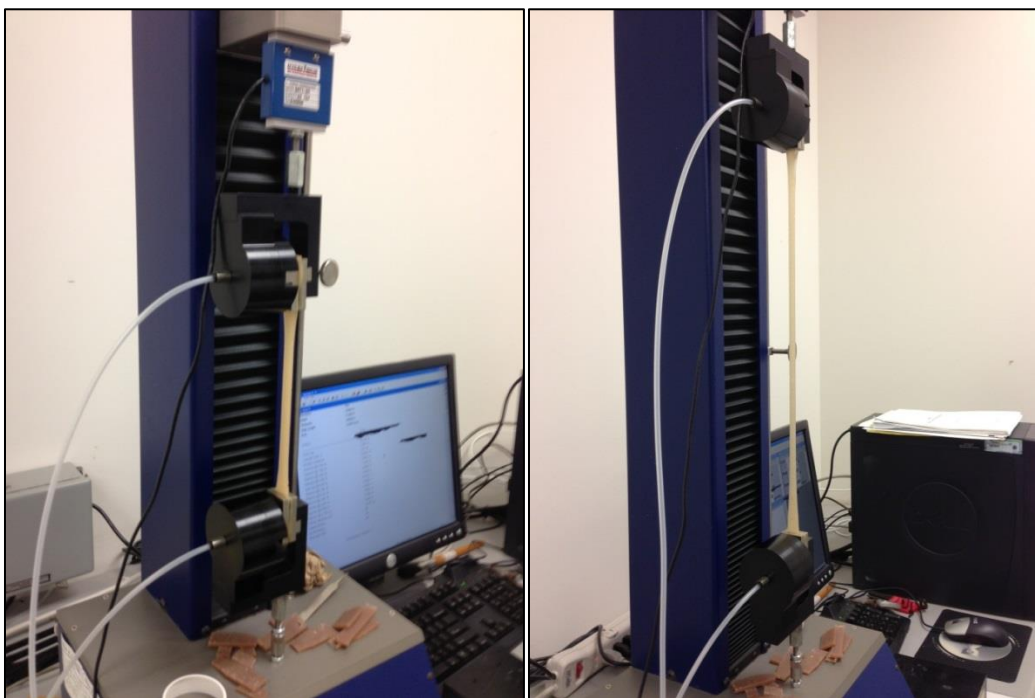


Figure 11: Flex 40 material specimen undergoing tensile testing at approximately 200% and 400% strain.

Figure 12 shows the Flex 40 "dog bones" after their tensile test. The top specimen in the figure had very few bubbles within the material and broke near the middle where necking caused the true stress to be the highest. The other three specimens, however, all broke where there was a

midsize to small bubble of no more than 1-2 mm. This is evidence that the bubbles affect the local strength in the material, but no noticeable error trend is visible when comparing the stiffness of the specimens that broke at a bubble or not.

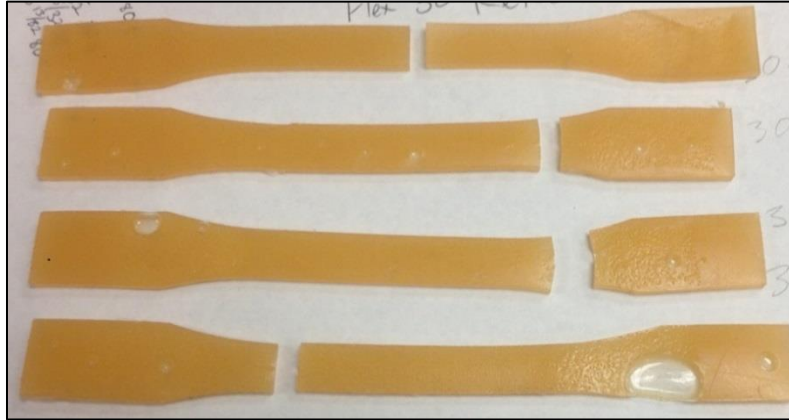


Figure 12: Flex 40 "dog bones" after material testing show breaks at bubbles present in the material.

The tensile test generated a load-displacement curve, shown in Fig. 13, that was converted into a stress-strain diagram. A linear regression determined the slope of the stress-strain curve, which graphically represents the modulus of elasticity.

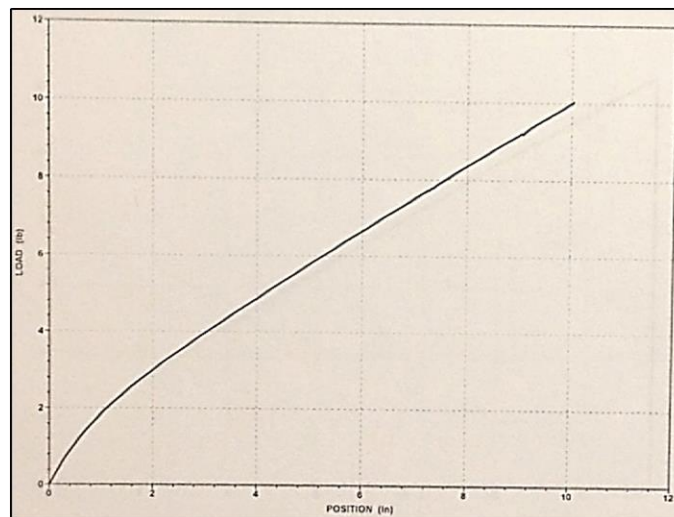


Figure 13: Load-displacement plot from the tensile test for the Flex 40 Alumilite material.

For the Alumilite materials, as with most elastomers, the actual modulus of elasticity is not as well defined as solid materials such as steel or aluminum. Especially at low strains, the slope of the load produced with respect to the deformation varies significantly. To determine the correct location on the curve to calculate the slope for the modulus of elasticity, the foils were approximated as a cantilevered beam in various loading configurations. The most conservative value for the maximum strain that should be seen in the material was used at .089 in/in. This is relatively low on the stress-strain curves shown in Fig. 14. Since the resolution of the material testing was not sufficient to give a confident answer for such a low strain, the next full order of

magnitude of strains were used in the regression to find the modulus of elasticity. The strains should still be reflective of the approximate value of the modulus. The relative difference in the calculated stiffness should not be affected by this technique, as any error will be consistent among the flexible materials.

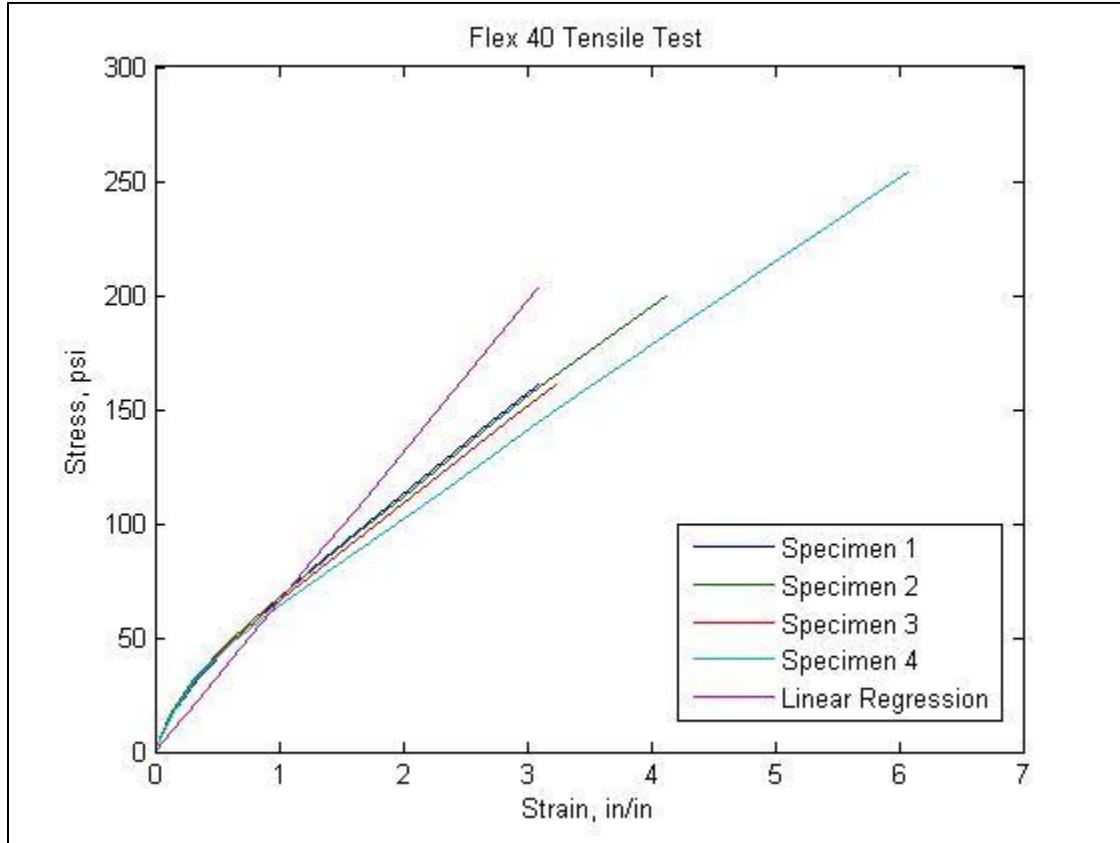


Figure 14: Stress strain diagram of Flex 40 material with linear regression to calculate the modulus of elasticity.

Table 1 provides the results of the material testing with the modulus of elasticity for each material. The Moduli span several orders of magnitude for the flexible materials and the rigid material is 2.3 orders of magnitude stiffer than the stiffest, Flex 80 foil. The manufacturer's comparison is provided by the Alumilite Corporation to give an idea of the approximate stiffness of the Flex materials.

Table 1: Foil Material Properties

Foil Material	Modulus of Elasticity (Pa)	Manufacturer Comparison
Rigid	3.00E+09	N/A
Flex 80	1.45E+07	Roller Blade Wheel
Flex 70	7.20E+06	Car Tire
Flex 60	2.13E+06	Shoe Sole
Flex 40	5.31E+05	Wine Cork
Flex 30	4.00E+05	Soft Rubber Gasket

All of the material properties were calculated from tensile tests that were pulled at 0.1 inches per second, except for the rigid material, which was pulled at 0.01 inches per second. Because the materials are elastomers, there is likely strain-rate dependence in their tensile properties. Depending on the amount of bend in the foils during their experimental evaluation, the strain rate of the material should have a maximum between 0.025 and 0.5 strain per second. Although further testing would be required to determine whether the rate at which the strain is applied to the flexible materials is significant, the strain rate tested is within the range of expected strain rates seen in the foil oscillations. If a strain-rate dependence is eventually quantified, it can be retroactively applied to the analysis because it should only affect the calculated Stiffness Constant.

D. Load Cell

The six-axis load cell, shown in Fig. 15, is configured with internal strain gauges to measure forces and torques in the x , y , and z directions. The forces of interest during the experiment were the x and y forces which were transformed into the lift and thrust forces depending on the instantaneous angular position of the foil. These forces determined the power out and efficiency of the propulsor. In the z -axis, the load cell measured the torque on the propulsor shaft, which was integrated with the rotational velocity to determine the power in and efficiency. While only these three outputs were paramount to the analysis, all six axes of the load cell were recorded for each run to compensate for crosstalk between the axes within the load cell. A heavy duty load cell with a rated moment tolerance of 700 N-m is used to withstand the strong moments that act on the propulsor during testing. A sampling rate of 300 Hz resolved the forces and torques measured throughout the entire cycle of oscillation, which do not go above 4 Hz. The load cell came factory calibrated and was verified using a spring-scale pull test.



Figure 15: Load cell used to measure forces and torques on the shaft with amplifier box and connecting cable.

E. Motor

The motor, shown in Fig. 16, manipulated the angular position of the propulsor using a proportional/integral/derivative (PID) controller with a sine wave programmed as the commanded input. The device used a 480V powered iterative feedback loop so that the motor oscillated the foil with minimal lag by adjusting the torque on the shaft as necessary to counteract the forces in the surrounding fluid. The feedback loop circuitry runs between 2 MHz and 8 MHz to provide high resolution positioning and rotational velocity control throughout the oscillation. The motor shaft has a key that allows it to transmit torque to the foil, and the inside of the shaft is threaded to allow a bolt to be used to secure the load to the shaft. The motor was configured to output a voltage value proportional to its relative position, which was recorded for the analysis and used to transform the forces and torques measured by the load cell to determine lift, thrust, power, and efficiency. The motor also issued triggers to the PIV system to synchronize the capture of images with specific angles in the oscillation.

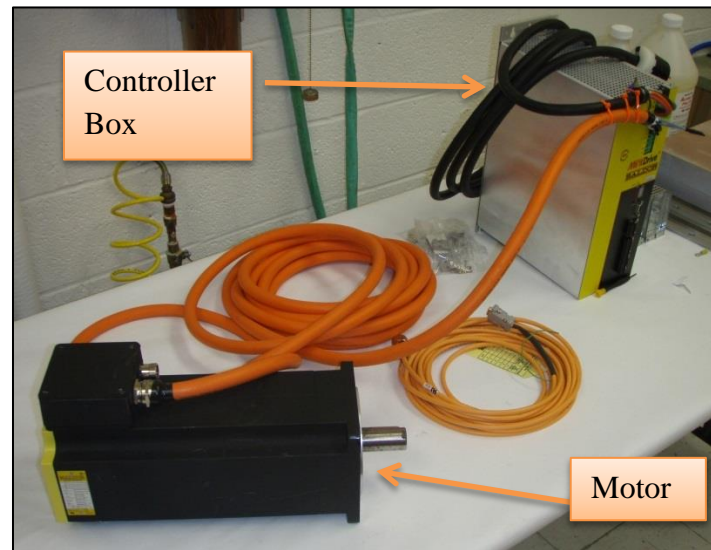


Figure 16: Motor for manipulating the angular position of the foil and controller box.

Initial data collection and analysis indicated that when the motor was run below approximately 2 Hz, the shaft would not smoothly oscillate due to motor cogging caused by the permanent magnets favorably aligning with the stator windings. The variable torque caused by the cogging is more prevalent when there is low or no current in the stator windings, which was the case for the low frequency oscillations that require less effort from the motor. The experiments were adjusted to only use oscillation frequencies between 2 Hz and 4 Hz, which reduced the prevalence of the cogging. The power in the motor makes it capable of nominal oscillation frequencies much higher than those used in the testing, but those capabilities were not tested because of their impracticality for application in engineering systems and the potential to damage the testing equipment including the load cell and foil due to the magnitude of the forces. The angular amplitude selected for all the tests was based on what previous research and computer simulations indicate was the optimal angle for oscillating propulsors. Because the flow had a

finite cross-section, the angular amplitude was also limited to prevent significant blockage of the fluid flow in the channel.

F. Mounting Apparatus

Figure 17 shows the schematic drawing of the pieces required to create a nearly rigid, electrically isolated connection between the motor and the foil. The apparatus mounts the motor on the sides of the water channel, connects through the load cell, and holds the foil in the proper position within the test section.

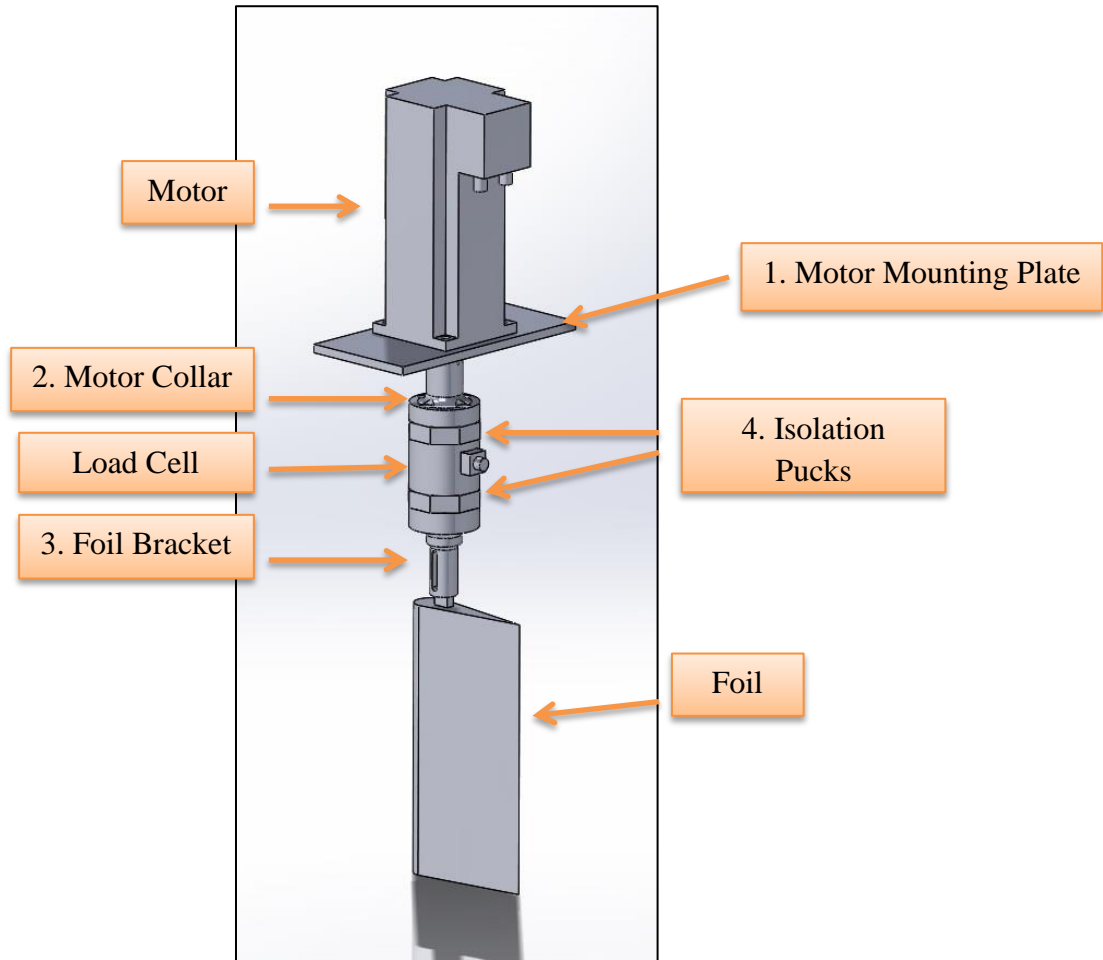


Figure 17: Drawing of the testing apparatus that was outfitted into the water channel.

1. Motor Mounting Plate

The motor mounting plate, specified in Fig. 18, is a 7" x 14" x 1/2" steel plate with a 1/8" depression that holds the 1/8" ring extension on the base of the motor (visible in Fig. 22 below). There are also four bolt holes that line up with the motor's mounting holes. A hole in the center of the mounting plate allows the motor collar to come up and attach to the motor shaft from below. The mounting plate had minimal contact with the water in the channel so corrosion was not a concern for the plain carbon steel.

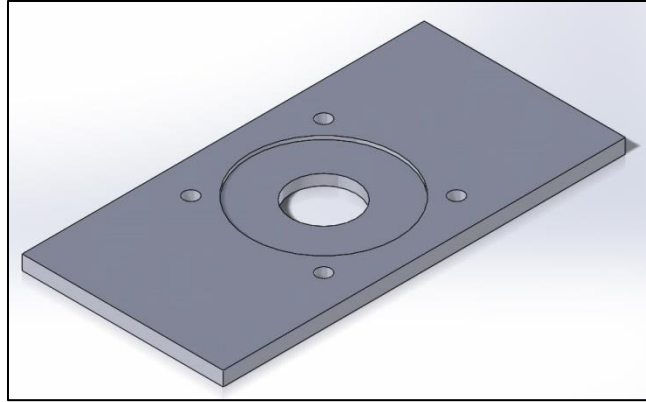


Figure 18: Drawing of the motor mounting plate, which secures the motor to the water channel.

Figure 19 shows the steel mounting plate in place atop the entire mounting apparatus without the motor in place. The motor collar is seen extending up from the foil, bracket, and load cell, and comes flush with the lower surface of the depression on the mounting plate.

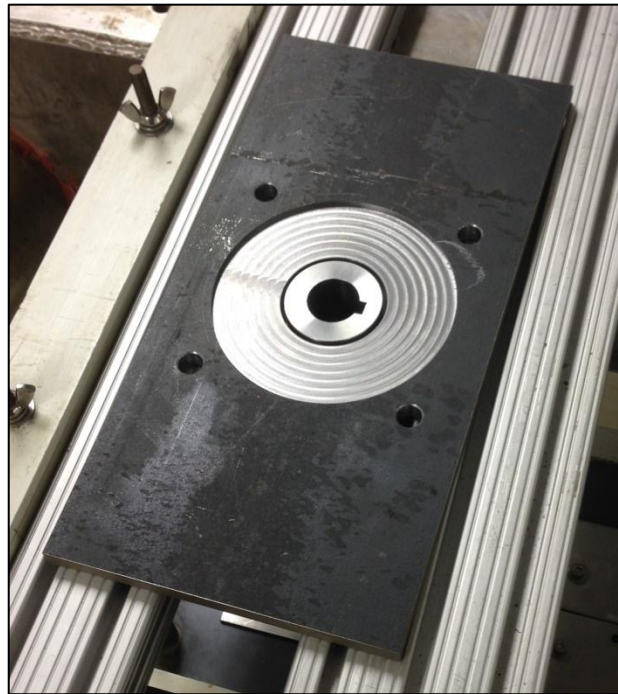


Figure 19: Testing apparatus without motor in place showing the motor collar extending through the mounting plate.

The mounting plate was bolted into and held up by two, 1½" 80/20 brand, extruded aluminum beams, which bolt into the side of the water channel. The 80/20 beams were initially resting directly on the water channel sides, but they had to be propped up another 2" by square steel pieces, shown in Fig. 20, to account for the additional height required with the inclusion of the isolation pucks. The slots in the 80/20 beams allowed for adjustments in the position of the motor laterally above the water channel. Additional play of about ¼" was available in the longitudinal direction since the 80/20 beams were raised up, and the bolt holes no longer needed to be perfectly concentric for the bolts to tighten down.



Figure 20: Motor apparatus propped up by 2" square bars accounting for height of the isolation pucks on the load cell.

2. Motor Collar

The motor collar design in Fig. 21 takes advantage of the key on the shaft of the motor with a keyway that accepts the majority of the torque applied from the motor. The collar fits tightly on the motor shaft, and two 10-24 set screws tighten onto the surface of the key to prevent the collar from slipping down the shaft while the collar is being fitted onto the motor. The large fillet at the transition from the smaller to larger diameter prevents a large stress concentration that could affect the material integrity during high frequency and high torque oscillations. The piece was made out of stainless steel for its rigidity, strength, and corrosion properties.

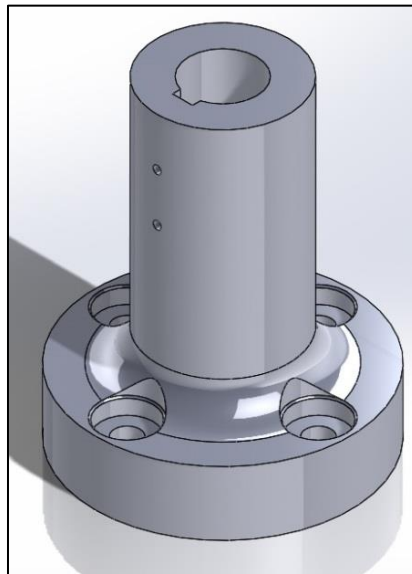


Figure 21: The motor collar attaches to the motor shaft and transmits torque to the rest of the testing apparatus.

The collar was designed to extend through the hole in the mounting plate to attach to the motor with a small gap to prevent friction between the collar and motor. Figure 22 shows the motor collar attached to the shaft of the motor with a small gap between its upper surface and the motor.



Figure 22: Motor collar attached to motor next to mounting plate.

With the load cell and foil attached, the set screws that tighten onto the motor shaft were not enough to hold the entire weight while the motor was oscillating. Thus, the motor collar was modified to take advantage of the threading inside of the motor shaft, which accepts a $\frac{1}{2}$ " bolt. A small puck rests on a lip, shown inside the collar in Fig. 23, and is held up on the $\frac{1}{2}$ " headless bolt by two nuts that lock into position to hold the apparatus at the correct height. The double-nut configuration allows the collar to be adjusted vertically to close the gap between the bottom of the foil bracket and the top of the grounding board.

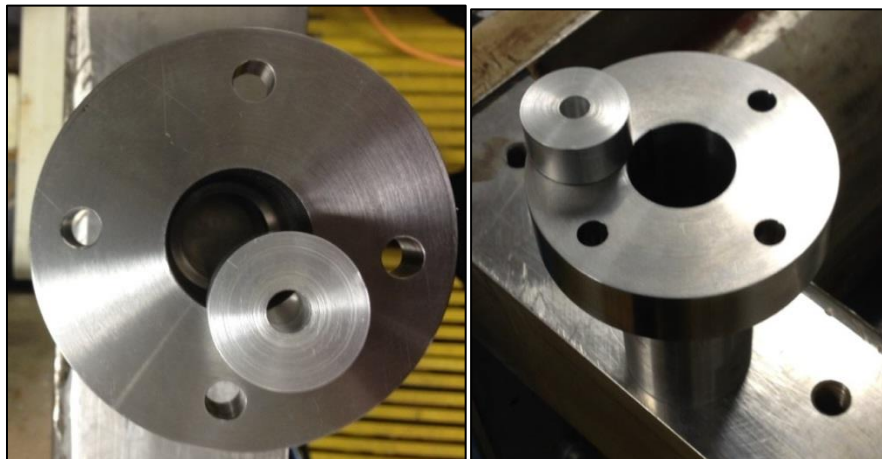


Figure 23: Amended collar design to allow utilization of the motor shaft's interior threading.

3. Foil Bracket

The foil bracket design, shown in Fig. 24, serves as a transition from the load cell to the foil. At its top, a hole pattern allows the bracket to screw into the bottom of the load cell. At the bottom, a 1" x ½" rectangular hole accepts the aluminum shaft from the backbone of the foil. While designs having only three of the four sides of the rectangle in place were considered, they were ruled out in favor of having a snug fit that would ensure rigidity between the load cell and foil. The bracket, like the collar, contains a large fillet to prevent stress concentrations during oscillations. The piece was also made out of stainless steel for its rigidity, strength, and corrosion properties.

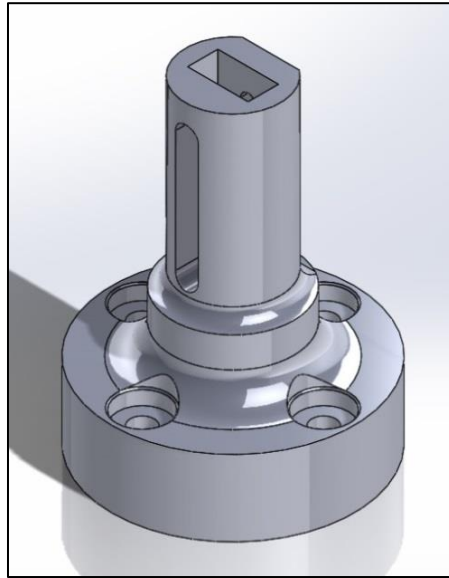


Figure 24: Drawing of the foil bracket that serves as a transition from the load cell to the foil.

To account for slight differences in the total height of the foils due to imprecise vertical placement of the backbone during pouring, the bracket incorporates a slot that allows the screws through the backbone to adjust vertically about ½" in each direction. To ensure that the foil does not slip during oscillations, the slot on the side with the head of the bolt is slightly wider, as shown in Fig. 25. This makes the clamping action of the bolt tighten the flat face of the backbone to the interior face of the bracket rather than relying on the head of the bolt alone for enough friction to hold the foil in position.

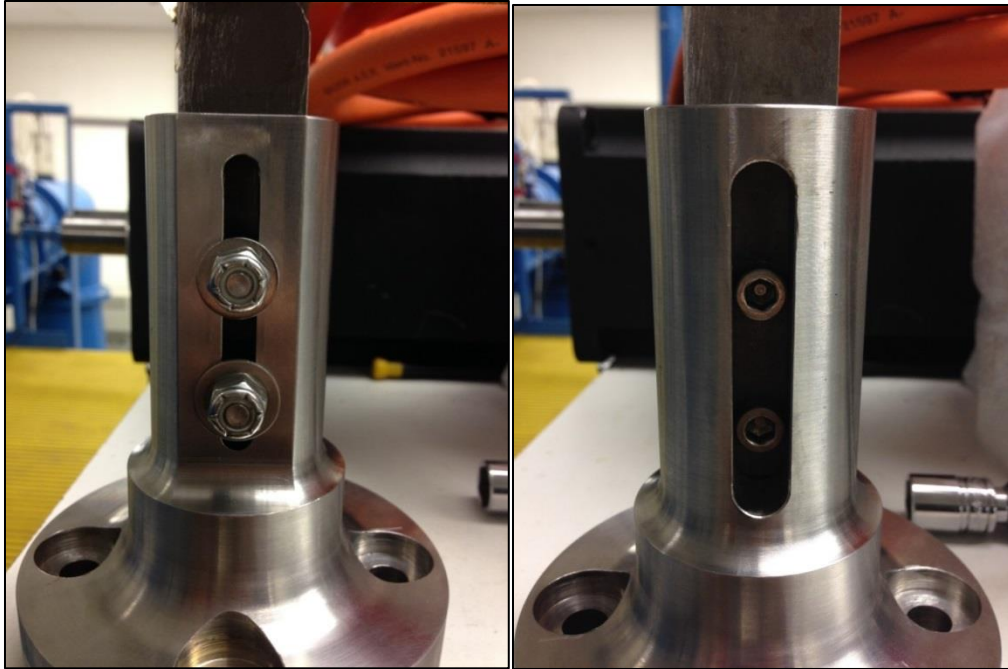


Figure 25: Both sides of the foil bracket showing the adjustable bolts holding the aluminum backbone in place.

4. Isolation Pucks

In preliminary testing of the apparatus, with the collar and bracket in direct contact with the load cell, the activation of the motor caused an offset in the forces and torques measured by the load cell. These offsets were sometimes up to 0.5 Volts, which corresponds to approximately 50 N. Troubleshooting the load cell in various configurations revealed that the majority of the offset was due to the electrical connection between the motor and the load cell. When the load cell was isolated electrically from the motor, the offset disappeared almost entirely. To isolate the load cell electrically, two pucks of G-10 were fabricated to accept the bolt pattern in place on the bracket and collar, and screw into the bolt pattern of the load cell with separate, electrically isolated bolts. This required the two bolt patterns to be at a 45° offset, as shown in Fig. 26.

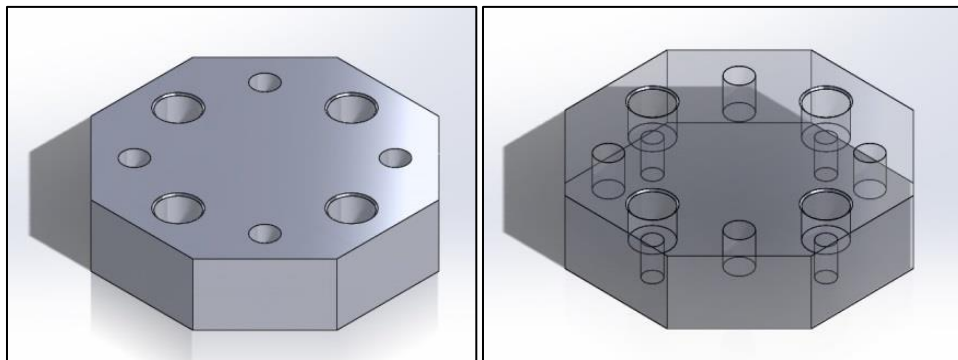


Figure 26: Isolation puck and transparent view of hole pattern with 45° offset to electrically isolate the load cell.

The attached G-10 isolation pucks also increased the total length of the transition apparatus from the foil to the motor by 2", as shown in Fig. 27. This extension required the motor to be raised up 2", as shown in Fig. 20.



Figure 27: Isolation pucks attached to either side of the load cell to prevent electrical interference.

Parameter Space

To fully investigate the range of non-dimensional parameters, a test matrix was used to define the dimensional parameter space to be used for the tests. The maximum and minimum dimensionless parameters and independent variables used for the analysis, provided in Table 2, were determined based on evaluations of current literature and research on pitching propulsors as well as some limitations of the testing apparatus. Within these ranges, it was expected that local peaks in thrust and efficiency would be found at intermediate values of the Strouhal Number and Stiffness Constant ranges in Table 2. Based on previous research, the extremes of these values were not expected to perform as well as the intermediate values in terms of thrust and efficiency. Increased resolution may be required for a full analysis of performance characteristics near significant points in the parameter space. For example, fluid dynamics has identified Reynolds Number around 5×10^5 as a region of interest where the flow transitions from laminar to turbulent. Additional research has shown that the majority of underwater organisms using this type of propulsion display motion with a Strouhal Number in the range of 0.2 to 0.4 (Rohr, 2004). It is expected that this range of Strouhal Numbers will see the highest efficiencies or thrust production (Rohr, 2004).

Table 2: Dimensionless Parameter Space

		Minimum Value	Maximum Value
Independent Variables	Flow Velocity, m/s	0.1	1.5
	Oscillation Frequency, Hz	2	4
	Modulus of Elasticity, Pa	4×10^5	3×10^9
Dimensionless Parameters	Reynolds Number, Re	3×10^4	3×10^5
	Strouhal Number, St	0.1	1.5
	Stiffness Constant, K	1×10^{-1}	6×10^4
	Swept Length, S	1.5	1.5

Within these values, the parameter space was developed in the matrix in Fig. 28. The Reynolds Numbers for the tests were first specified on a logarithmic scale to naturally space the testing along the entire order of magnitude that the Reynolds Number spans. With the density, chord length, and viscosity being otherwise constant, the only parameter that varied along with the Reynolds Number, specified in Eq. (1), was the free-stream velocity. The velocities required to meet those Reynolds Numbers were determined and listed on the left side of the matrix. The next parameter to be accounted for was the Strouhal Number, which varies by both frequency and velocity in Eq. (2). With the velocities already coordinated to specific Reynolds Numbers, frequencies were chosen that would satisfy Strouhal Numbers between 0.1 and 1.5. This created a 7x8 matrix of Strouhal Numbers for each combination of oscillation frequency and channel velocity. These 56 Strouhal numbers were run with each of the six foils, which resulted in the Stiffness Constants located in the right side of the matrix depending on the flow velocity and the foil's modulus of elasticity, as specified by Eq. (3). With each of the six foils running the 7x8 matrix of Strouhal Numbers, 336 unique tests could be run to explore the entire parameter space. To account for outliers in the data and increase the statistical confidence in the results, each point in the parameter space was run at least twice.

Trident Project Parameter Space									Flex 30	Flex 40	Flex 60	Flex 70	Flex 80	Rigid						
15-Jan-14									Frequency (Hz)						Modulus of Elasticity (Pa)					
									2.00	2.21	2.43	2.68	2.96	3.26	3.60	4.00E+05	5.31E+05	2.13E+06	7.20E+06	1.45E+07
Re=pVc/μ	Velocity (m/s)	Strouhal Number (St=fL/V)							K=EI/.5pV^2c^3											
3.29E+04	0.1876	0.737	0.812	0.896	0.988	1.090	1.202	1.326	7.39E+00	9.80E+00	3.93E+01	1.33E+02	2.68E+02	5.54E+04						
4.38E+04	0.25	0.553	0.610	0.672	0.742	0.818	0.902	0.995	4.16E+00	5.52E+00	2.22E+01	7.49E+01	1.51E+02	3.12E+04						
5.84E+04	0.3331	0.415	0.458	0.505	0.557	0.614	0.677	0.747	2.34E+00	3.11E+00	1.25E+01	4.22E+01	8.49E+01	1.76E+04						
7.79E+04	0.444	0.311	0.343	0.379	0.418	0.461	0.508	0.560	1.32E+00	1.75E+00	7.02E+00	2.37E+01	4.78E+01	9.89E+03						
1.04E+05	0.5916	0.234	0.258	0.284	0.313	0.346	0.381	0.421	7.43E-01	9.86E-01	3.96E+00	1.34E+01	2.69E+01	5.57E+03						
1.38E+05	0.7884	0.175	0.193	0.213	0.235	0.259	0.286	0.316	4.18E-01	5.55E-01	2.23E+00	7.53E+00	1.52E+01	3.14E+03						
1.84E+05	1.0506	0.132	0.145	0.160	0.176	0.195	0.215	0.237	2.36E-01	3.13E-01	1.25E+00	4.24E+00	8.53E+00	1.77E+03						
2.46E+05	1.4	0.099	0.109	0.120	0.132	0.146	0.161	0.178	1.33E-01	1.76E-01	7.06E-01	2.39E+00	4.80E+00	9.95E+02						
									Angle (°)	μ (N-s/m^2)	L (m)	c (m)	b (m)	w (m)	I (m^3)	ρ (kg/m^3)				
									15	1.01E-03	6.91E-02	0.178	0.4	0.028	1.83E-06	998.2				

relative to the flow using the instantaneous angle of attack of the foil. These forces are non-dimensionalized into the Coefficient of Drag (C_D) and Coefficient of Lift (C_L),

$$C_D = \frac{F_D}{\frac{1}{2}\rho V^2 cb} \quad (5)$$

$$\text{and} \quad C_L = \frac{F_L}{\frac{1}{2}\rho V^2 cb}, \quad (6)$$

where F_D is the drag force, F_L is the lift force, ρ is the fluid density, V is the free-stream velocity, c is the foil chord length, and b is the foil span. A negative Coefficient of Drag means that the propulsor is producing thrust opposing the drag from the fluid. Because of the equal and opposite relationship of thrust and drag in this experiment, the thrust was conventionalized as a positive force to simplify the analysis of collected data and reflect the goals of the experiment.

The torque from the load cell was integrated over a full period of oscillation with the instantaneous angular velocity to determine the power being put into the system by the motor (P_{in}). The thrust was also integrated over a full period of oscillation with the free-stream velocity to determine the power out (P_{out}). The power in and power out are used to determine the efficiency (η), specified by

$$P_{in} = \frac{1}{T} \int \tau \omega dt, \quad (7)$$

$$P_{out} = \frac{1}{T} \int F_T V dt, \quad (8)$$

$$\text{and} \quad \eta = \frac{P_{out}}{P_{in}}, \quad (9)$$

where T is the period of foil oscillation, τ is the shaft torque, ω is the angular velocity, t is time, F_T is the thrust force, and V is the free-stream velocity.

Figure 29 shows the force measured from the load cell plotted in the time domain for a high efficiency oscillation of the Flex 30 propulsor. Because the time domain plot is difficult to read and interpret, the forces were instead plotted against the angular position of the foil. This made it easier to see the forces generated including where in the cycle the most thrust and lift were produced. The precision of the overall testing apparatus could also be assessed based on the consistency of the plots without worrying about synchronizing the time domain runs by adjusting the time scale of the data.

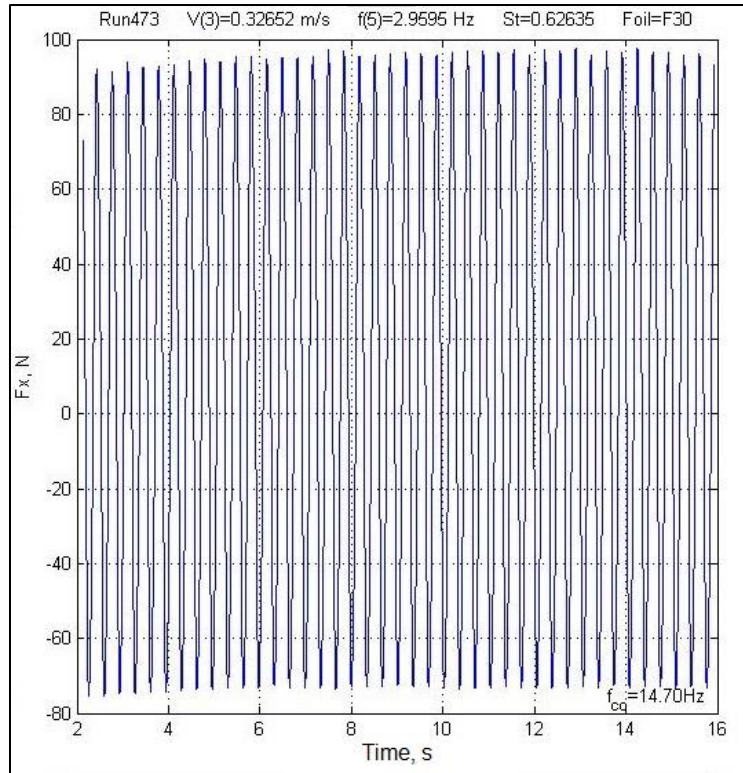


Figure 29: Time domain results for the force in line with the foil for a high efficiency run of the Flex 30 propulsor.

The initial data collected showed that the apparatus could produce repeatable results within a reasonable margin of error. Figure 30 shows the force measured by the load cell relative to the angular position during three different runs involving the same flow speed, foil stiffness, and oscillation frequency, but collected weeks apart. The differences in the various results reflect varying filtering methods, motor parameters and configuration, and water channel flow speed. Each test consisted of about 30 seconds of data that plot very consistently over itself for each run. The slight differences in setup between the different runs were not a factor during the duration of the individual run.

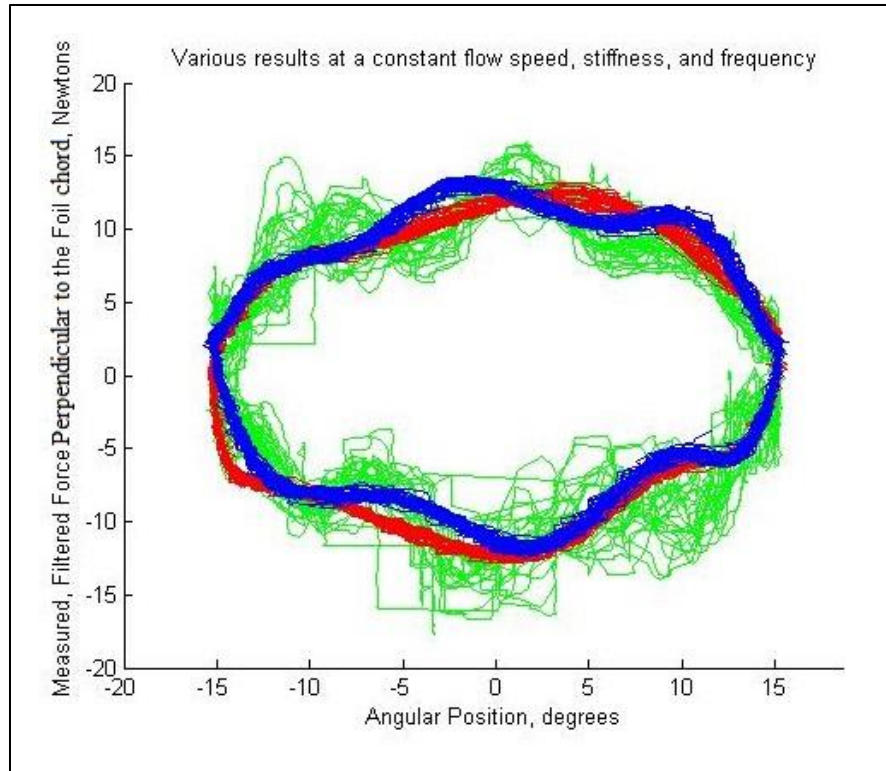


Figure 30: Force measured perpendicular to the foil face at a constant flow speed, stiffness, and frequency in separate oscillations.

While Fig. 30 shows the repeatability of the results for given input parameters, it also shows a significant problem with the initial setup used to provide oscillations to the foil. Ideally, the measured force perpendicular to the foil would see one dominant peak and trough per cycle, which corresponds to the equal and opposite forces on the foil as it pushes through the water at its maximum angular velocity. Between the peaks and troughs, the force should gradually drop through zero near the maximum extent of the oscillations as the foil stops and proceeds in the opposite direction. This would produce an ovular shape as the force traces counterclockwise through its maximum, minimum, and respective zeros. Figure 31, however, shows several additional oscillations in the measured data that cause the force to have several other local peaks during the oscillation. The cause of these additional peaks was identified as the motor shaft cogging rather than moving smoothly through the oscillations. This cogging is caused by the preferred alignment of the permanent magnets in the motor to the metal in the stator windings. This behavior is common among high power, DC brushless motors, especially when performing motions that require only a small percentage of their maximum capabilities. In motion profiles that require more effort, the power into the motor can more easily overcome the preferred alignment and move smoothly between specified angles.

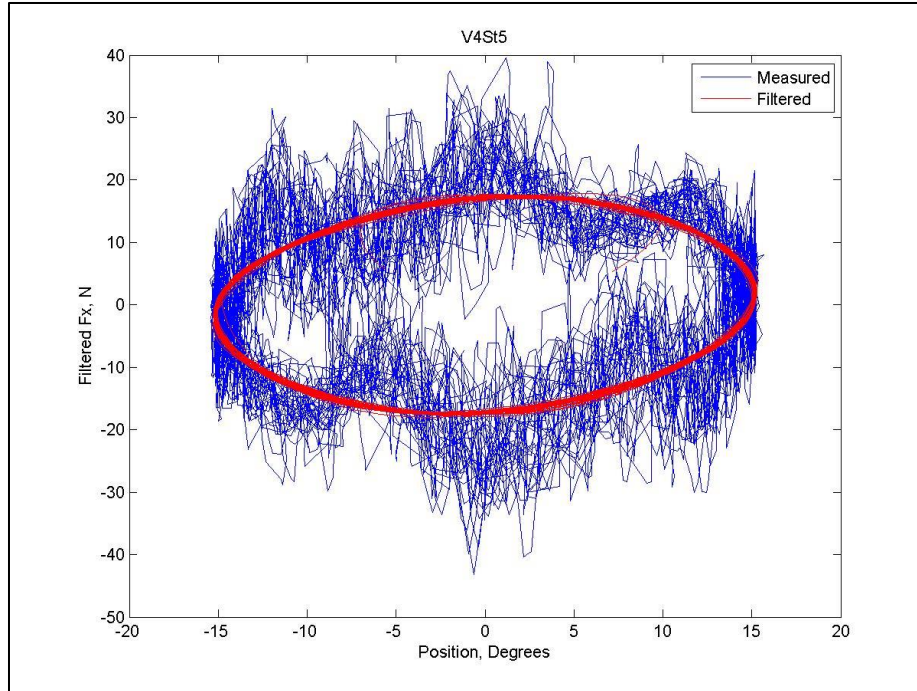


Figure 31: Force measured perpendicular to the foil before and after application of a low pass filter.

To reduce the perceived effect of the cogging, a software-based low-pass filter with a cutoff frequency five times the dominant oscillation frequency was applied to the data. However, it could not be assumed that the cogging was not having a significant effect on the overall performance of the foil during oscillations. For example, Fig. 31 shows the original, unfiltered data alongside the filtered data for one of the runs in Fig. 30. This type of filtering makes the data appear in a shape similar to what is expected for the run. It has two peaks, one positive and one negative, and the rest of the data points continuously approach the opposite peak with no intermediate local peaks. While the qualitative analysis of the filtered data appears to align with the expected trends, the quantitative analysis could not be considered reliable.

To mitigate the potential physical effects of the motor cogging, the parameter space was adjusted to utilize higher oscillation frequencies. Because of the size of the motor used, running at higher frequencies reduced the presence of the cogging, which was likely due to low torque demands being unable to overcome the cogging torque. The motor also became easier to tune for higher frequency oscillations. The increased frequency corresponded to an increase in the required flow speed to achieve the same range of Strouhal Numbers. In addition, the combined increase in flow speed and frequency increased the forces measured by the load cell during oscillations. While the inertial forces measured from the cogging decreased, the forces measured from the desired physical phenomena increased. The increased signal-to-noise ratio increases the statistical confidence in filtering out the high frequency content of the data. Oscillations where the forces did not significantly increase relative to the noise caused by the cogging were associated with extreme negative efficiencies due to the lack of thrust produced. Thus, the only

parameter space that remained affected by the cogging was not paramount to the results of the experiment.

To apply the low-pass filter, the data were first converted into the frequency domain using a fast Fourier transform. The frequency domain of the data collected from the most flexible foil, Flex 30, is plotted in Fig. 32 alongside the filtered frequency plot. The largest peak frequency is equal to the oscillation frequency of approximately 2.96 Hz. Additional harmonics of the oscillation frequency appear as significantly large peaks, indicating the presence of phenomena that happen multiple times per oscillation of the foil. Examples of such phenomena include the generation of thrust as the foil oscillates from one side to the other and back again, all in one cycle, or the delayed thrust generation seen in the flexible foils, which would create an extra oscillation per half cycle. To include all of these data up to the fourth harmonic, the cutoff frequency was chosen as the fifth harmonic. All frequency values above the cutoff frequency were set to zero, and the filtered data were then converted back to the time domain.

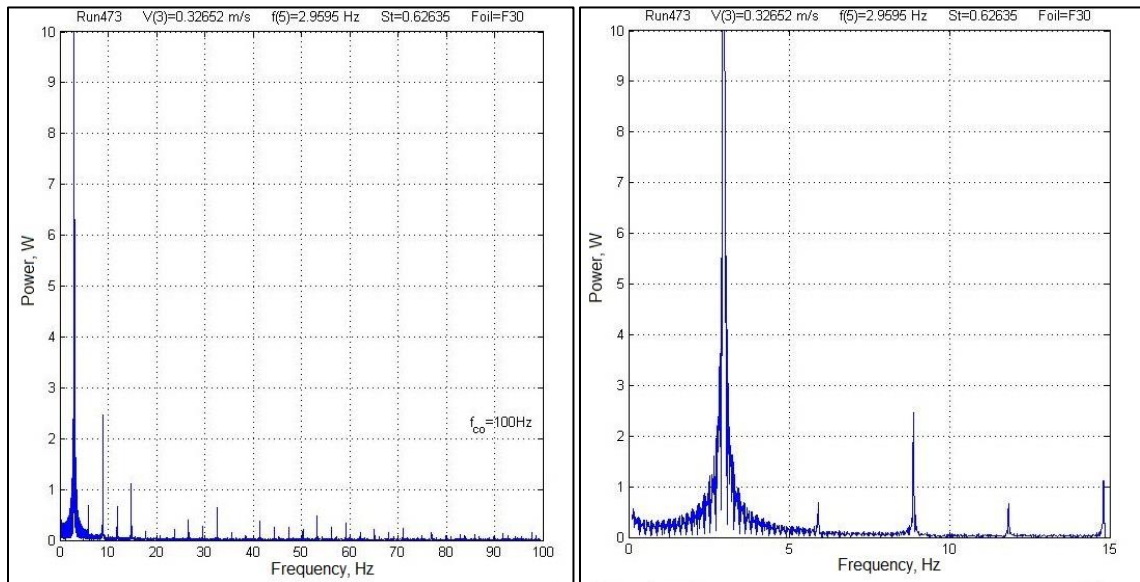


Figure 32: Unfiltered and filtered force data in the frequency domain with zeroed values above the cutoff frequency.

Figure 33 shows the same Flex 30 frequency data from Fig. 32 converted back to the time domain and plotted against the angular position of the foil. The various plots are from before and after filtering as well as the result of filtering the data at too low a cutoff frequency. The unfiltered results show significant extra oscillations resulting from the motor shaft cogging. When filtered using the cutoff frequency of five times the oscillation frequency, the majority of the cogging noise is removed, and the overall shape and values of the plotted data remain the same. As the filter cutoff frequency further decreases to three times the oscillation frequency, the noise continues to decrease. Unfortunately, along with the noise reduction, the characteristic shape of the plot changes, the values of the peaks decrease, and the angular positions at which the peak forces are measured change.

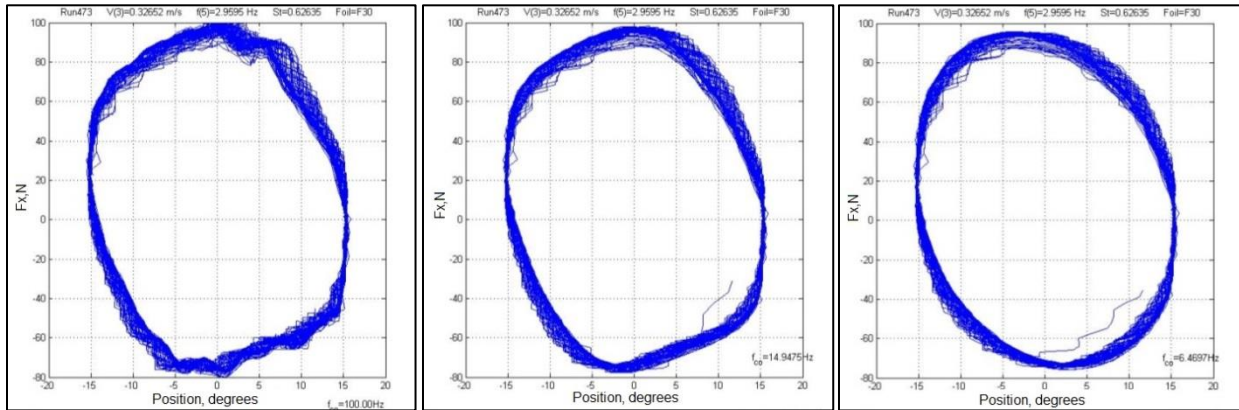


Figure 33: Unfiltered, filtered, and excessively filtered force data perpendicular to the foil.

The forces in line and perpendicular to the foil chord had to be transformed into the streamwise thrust and perpendicular lift forces based on the instantaneous position of the foil after the force data were recorded. Figure 34 displays the transformed data represented as the forces of thrust and lift for the same run as displayed in Figs. 32 and 33. When the foil is at the 0° position, the thrust and lift data directly transform to the measured forces in line and perpendicular to the chord of the foil. At the maximum oscillation angle of 15° , the smaller force in line with the chord has nearly no effect on the shape or values of the lift force plot. However, the large force acting perpendicular to the chord has a significant effect on the shape and magnitude of the thrust plot, which is transformed to the double-lobed shape shown in Fig. 34.

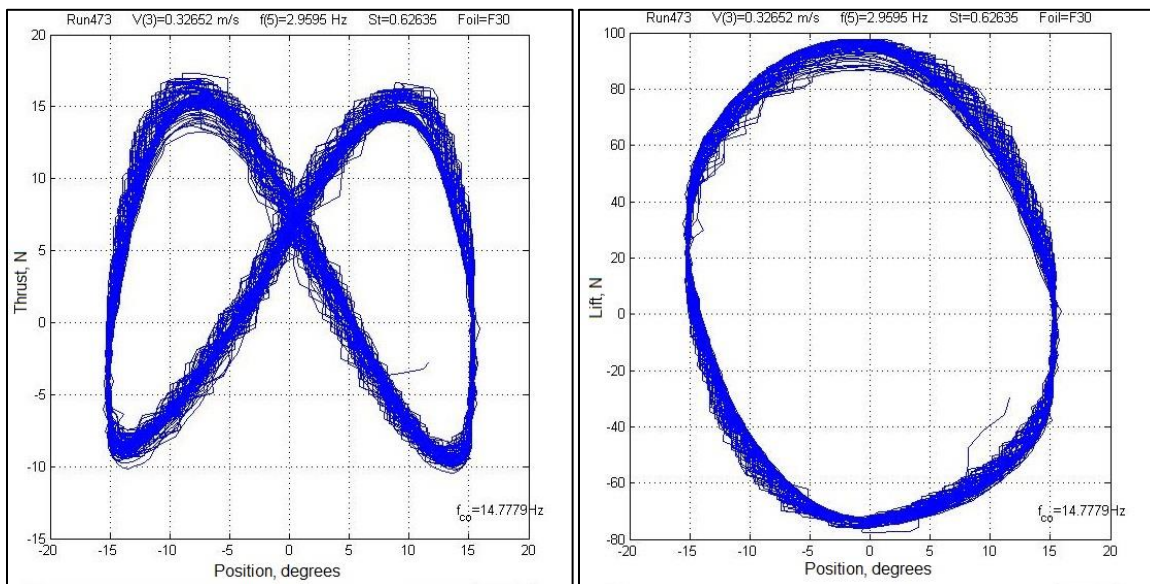


Figure 34: Transformed thrust and lift force data correlating to the direction of the flow.

The shape of the thrust plot reveals several important pieces of information about the oscillation performance. The peaks of the thrust plot lie at about 15 N while the lowest points only go down to about -10 N. The negative value of the thrust indicates that the fluid is pushing the foil

backwards along with the flow rather than forward against the flow. This is the result of drag on the foil as well as the force required by the foil to push into the flow to reach the maximum 15° angle on either side of its oscillation. However, because the foil is being considered as a propulsor attached to a vehicle rather than a vehicle itself, all negative forces are generically referred to as a drag that is innate to its oscillation through a flow. Regardless of naming convention, this asymmetry indicates that the foil generates higher thrust as it begins its swing than it creates drag at the end of its swing in each direction.

Because the power developed by the system, defined in Eq. (8), involves an integral of the thrust multiplied by the free-stream velocity, the amount of area above and below the zero force axis on the thrust plot is related to whether the oscillation had a positive or negative output power into the system. This is not a perfect correlation because the graphs do not indicate the angular velocity of the foil being highest near the 0° point and zero at the 15° point. Since the integral is taken with respect to time, the amount of time spent at any given force in the plot is significant. The forces at angles further from 0° will have a higher weight in the integral due to the lower angular velocity at those points. The graph still provides an initial look at the power performance of the propulsor as the sign of the power in turn determines the sign of the efficiency of the oscillation. In the case shown Fig. 34, the area above the zero force axis is visibly larger than the area below the axis. In this case, the efficiency is calculated to be 8.34%. The remaining power is lost due to unproductive water movement and mechanical losses.

In general, a higher proportion of area above the axis than below it corresponds to a higher efficiency, and a symmetry about the zero axis, with equal areas on either side, indicates an oscillation with zero efficiency. Figure 35 displays the thrust and lift plots for a lower Strouhal Number oscillation of the Flex 30 foil. Visibly, the thrust plot is nearly symmetrical about the zero-force axis, which corresponds to its -0.1% efficiency. Zero efficiency means that the foil is taking just as much power out of the fluid through drag as it is generating through its thrust production. Further increases in the area below the axis correlate with negative efficiencies that result in a net loss of power from the fluid.

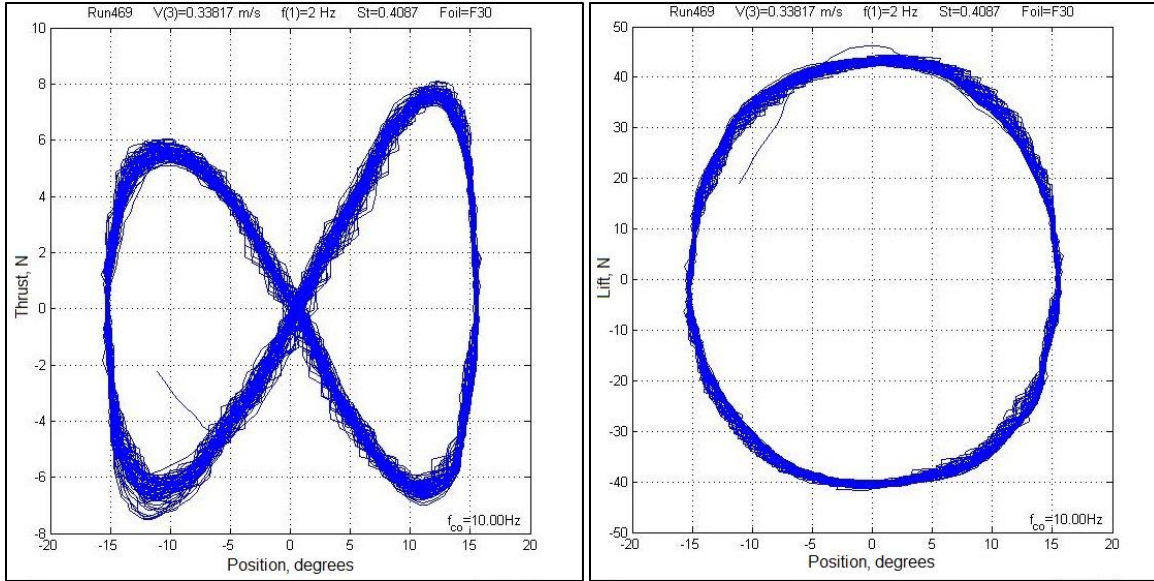


Figure 35: Thrust and lift forces from a lower Strouhal Number run with the Flex 30 foil resulting in -0.1% efficiency.

The amount of thrust produced by the foil for any given oscillation can be characterized by the Coefficient of Thrust described by Eq. (5). Figure 36 shows the Coefficient of Thrust calculated for each oscillation. The Thrust Coefficient for each foil follows an approximately exponential growth as the Strouhal Number increases. At the lowest Strouhal Numbers, some of the Thrust Coefficients are negative, which indicates that the foil is producing more drag than thrust in the oscillation. The negative Thrust Coefficient also corresponds to a negative efficiency. The trends seen in the data indicate that the most rigid foils produce greater thrust than the more flexible foils for any given Strouhal Number.

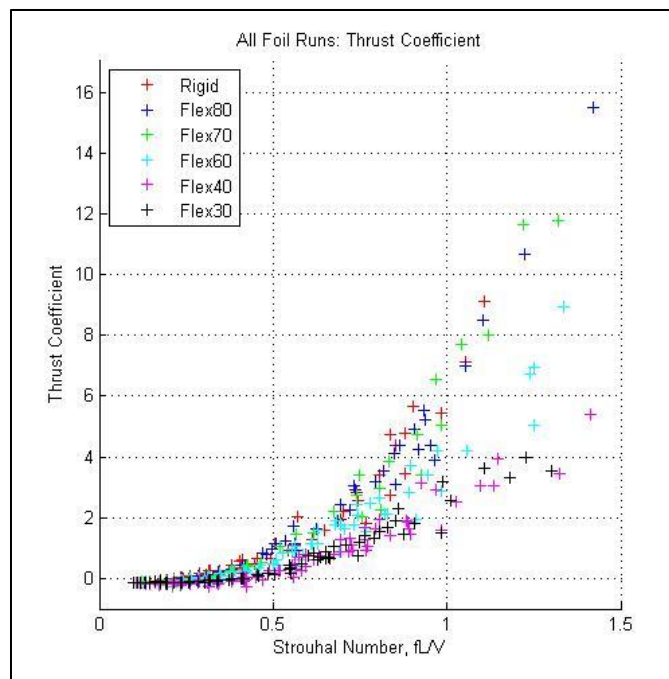


Figure 36: Calculated Coefficients of Thrust for the ensemble of foils.

While the thrust graphs can be compared visibly to determine relative performance, it is not possible to quantitatively determine the efficiency of the oscillation based on the thrust alone. The efficiency also takes into consideration the amount of power being put into the foil through an integration of the torque on the shaft multiplied by its instantaneous angular velocity. The torque data from the same oscillation as Figs. 32-34 are shown in Fig. 37. The torque on the shaft is due to the fact that the forces perpendicular to the foil chord act at a center of pressure behind the shaft axis, which results in a moment applied to the shaft. Because it is based on the perpendicular force, the torque plot is also roughly the same shape as the lift plot.

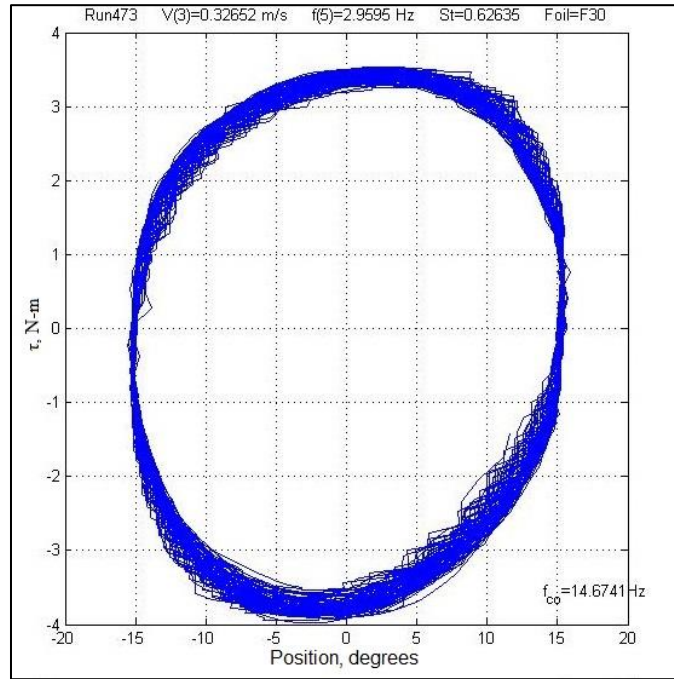


Figure 37: Shaft torque plotted against the angular position.

Figure 38 shows the plots of the torque multiplied by the angular velocity plotted against the angular position. The left plot is from the same 8.34% efficiency data set as seen in Figs. 32-34 and 37, and the right plot is from the zero efficiency run in Fig. 35. Visual analysis of these plots gives similar insights into the power being input into the foil through the shaft. For the high efficiency oscillation, the data trace through roughly the same path whether the foil is moving from its center position to its maximum angular position or vice versa. This pattern is primarily seen in runs with higher Strouhal Numbers where the velocity of the fluid is small compared to the frequency of the foil. The water is not moving fast enough to induce any significant additional drag on the foil due to its angular position.

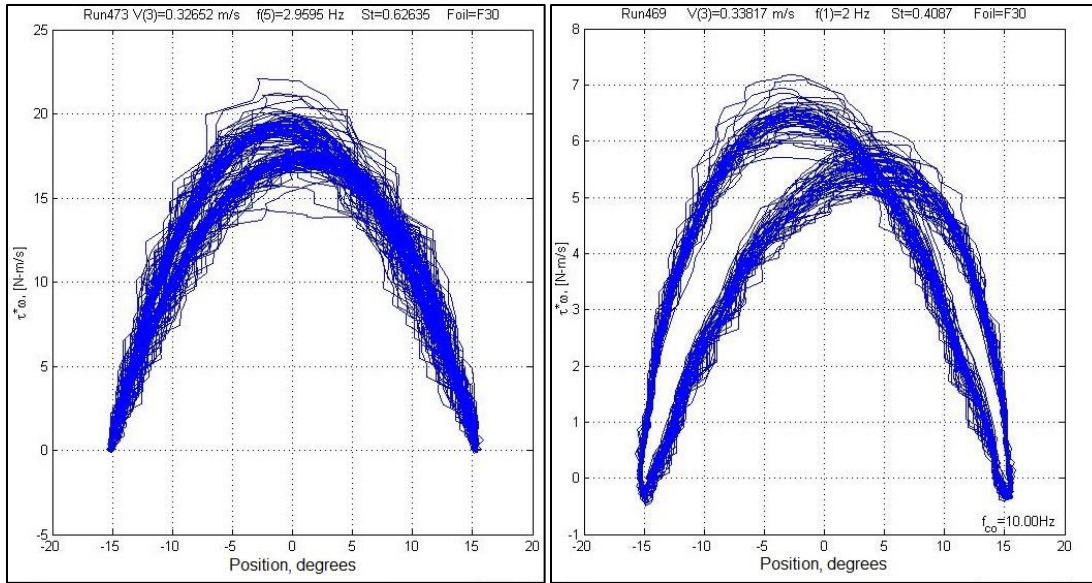


Figure 38: Shaft torque multiplied by angular velocity plotted against angular position showing different behavior and values for high (left) and low (right) Strouhal Number oscillations.

The right plot displays the shaft torque multiplied by its angular velocity from same zero efficiency case of the Flex 30 foil shown in Fig. 35. While the flow speed is approximately the same between the two cases, this oscillation has a lower frequency, which results in a lower Strouhal Number. In this case, the combined decreased angular velocity and resulting torque necessary to rotate the shaft result in values about one third of the previous case. The two arches also separate as a result of the maximum torque occurring earlier in the foil's swing from maximum angle to the zero angle. The lower relative torque is likely due to the foil not moving fast enough to sustain a positive pressure in advance of its angular swing. Any build up of pressure is washed into the wake before it continues to affect the foil. With the integrated torque multiplied by the angular velocity in the denominator of the efficiency equation, the larger values in these plots result in lower efficiencies for the same thrust outputs. The total efficiency can be increased by either increasing the power being output by the foil or decreasing the power input into the foil without changing the opposing power input or output power, respectively.

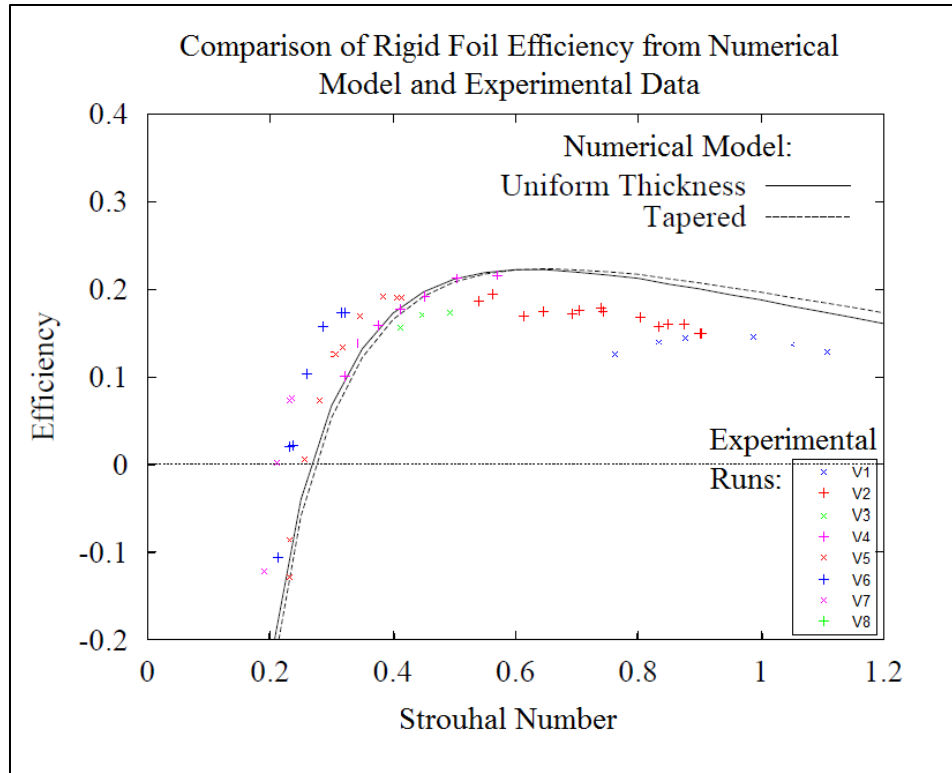


Figure 39: Efficiency for the rigid foil oscillations compared to the predictions from the numerical model (Murray, 1999).

Figure 39 compares the predicted results from the numerical model developed by Murray (1999) for the uniform thickness and tapered rigid propulsors. The V-numbers in the “Experimental Runs” legend correspond to each of the eight rows of the parameter space, which contains oscillations at different flow speeds. The general trends shown by both data sets are very similar. Both increase steeply from negative efficiencies, level out at a maximum efficiency, and slowly decrease linearly with increasing Strouhal Number. The experimental data show higher efficiencies before the maximum is reached and lower values after the maximum is reached. The maximum efficiency is also lower for the experimental data, but this maximum occurs at a lower Strouhal Number than predicted by the numerical model. While the numerical model does not perfectly predict the rigid foil performance, the experimental data show that the model can be used as an initial approximation for application of rigid propulsors.

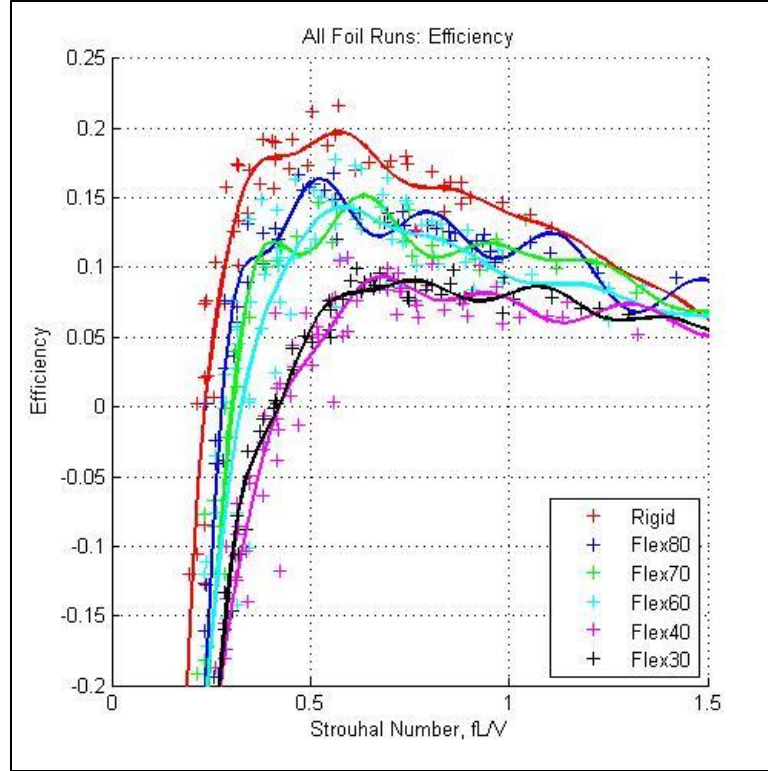


Figure 40: Raw efficiency calculated for the entire parameter space with overlaid spline functions fit to each foil.

Figure 40 shows the efficiencies plotted with their respective foils with an overlaid spline function fit to the raw data points. In general, the foils with the higher Stiffness Constants had higher efficiencies for any given oscillation observed. The rigid foil had the highest efficiencies out of all the foils. The Flex 80, Flex 70, and Flex 60 foils all appeared to have results clustered just below the rigid foil on the efficiency plots. The Flex 40 and Flex 30 foils also clustered together, but there was a gap between their efficiencies and the efficiencies of the other cluster of foils.

Table 3: Efficiency points of interest for each foil

Foil	Peak Efficiency, η	Strouhal at Peak η	Strouhal at Zero η	Post peak slope (η/St)
Rigid	21.69%	0.57	0.23	-0.16
Flex 80	16.77%	0.56	0.28	-0.09
Flex 70	14.70%	0.52	0.30	-0.08
Flex 60	17.81%	0.56	0.33	-0.12
Flex 40	12.74%	0.76	0.42	-0.10
Flex 30	9.94%	0.62	0.42	-0.05

Table 3 provides the approximate values of the maximum measured efficiency and its corresponding Strouhal Number, the Strouhal Number where the spline function crosses the zero efficiency line, and the slope of the efficiency data after the peak is reached. The efficiency trends are similar for each foil. As the Strouhal Number increases from values below 0.2, the

efficiency rises from extremely negative efficiencies. These low Strouhal Number oscillations show the biggest difference in efficiency performance between foils. For example, the same Strouhal Number that gives a efficiency of zero for the rigid foil gives a -50% efficiency for the Flex 30 and Flex 40 foils. Increases in Strouhal Number from 0.3 to 0.5 cause marginally smaller increases in efficiency as the trend lines become less steep. Depending on the foil, the maximum efficiency is reached at a Strouhal Number between 0.4 and 0.6. In general, the more rigid foils reach their maximum efficiency at lower Strouhal Numbers than the more flexible foils. As a result, the foils with the higher Stiffness Constants peak in efficiency at lower oscillation frequencies. With lower oscillation frequencies at the peak, there is less power required to be input into the foil, which in turn gives a higher efficiency. After the peak in efficiency, all of the foils show consistent decreasing trends in efficiency. The decrease for the more rigid foils, which have higher peaks, is steeper than the more flexible foils. If the trend continues at the same slope for increasing Strouhal Numbers, it is possible that there is a point that the efficiency of the most rigid foil would be less than all of the other foils. Further testing would be required at runs with high frequencies and low flow speeds. In general, these high Strouhal Number conditions would not be sustainable for an underwater vehicle because the vehicle would quickly accelerate, increase the relative speed of the flow over the foil, and decrease the Strouhal Number.

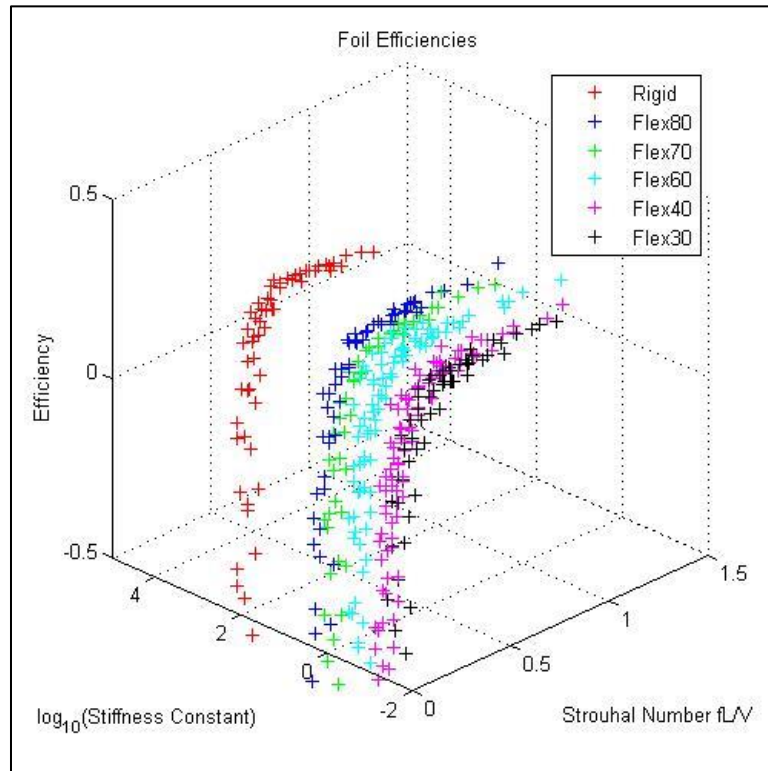


Figure 41: Three-dimensional plot of Strouhal Number, Stiffness Constant, and efficiency.

Figure 41 displays the same efficiency information, but with the Stiffness Constant plotted logarithmically on the third axis. Although there is a gap in the Stiffness Constants between the

rigid and Flex 80 foils, the data in general make a surface that has a near linear gradient causing a proportional increase in efficiency at any given Strouhal Number with a logarithmic increase in Stiffness Constant.

Particle Image Velocimetry Analysis and Results

As stated previously, significant details about the fluid-foil interaction can emerge from an analysis of the wake. To access this information, particle image velocimetry (PIV) was used to generate a velocity vector map of a layer of the fluid in the wake of the propulsor. PIV uses a high-speed camera and illuminating laser light sheet to capture the difference in position of seed particles in the fluid. This method was chosen for primary analysis over simpler flow visualization methods such as dye injection because it provides a quantitative analysis of the vorticity in the wake.

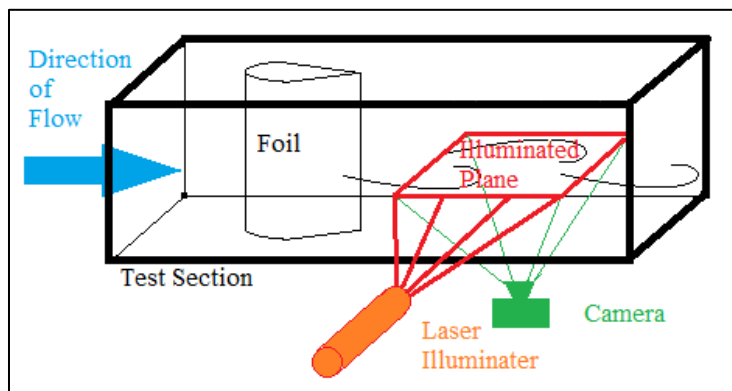


Figure 42: Schematic of particle image velocimetry data collection apparatus used to generate a vector field of the flow.

Figure 42 shows an overall schematic of the PIV behind the pitching propulsor. The camera and laser were oriented perpendicular to one another in a plane that is perpendicular to the direction of flow. The laser light illuminated the particles in a horizontal plane in the fluid behind the propulsor. The camera then captured two images of the illuminated particles in close succession. By calculating the distance and direction traveled by each particle in the layer, PIV algorithms calculated the velocity and vorticity fields in the wake as well as the number, types, and drift of the wake vortices. The 2D case using a full span model assumes that the parallel flow planes behind the foil are statistically the same. While this assumption loses accuracy near the top and bottom of the foil, testing the mid-span gives results closest to what would be seen in an ideal 2D case.

The PIV data provided additional information about the fluid-foil interaction that corroborated the forces produced and efficiencies calculated. Figure 43 shows three typical wake vortex configurations that were expected to appear from the PIV analysis. The negative efficiency case (top), known as the von Kármán vortex street, is characterized by alternating vortices where the vector sum between any two vortices is opposing the direction of flow. High velocities pointing in this direction contribute to an overall momentum deficit in the wake, which may be quantitatively related to the drag force on the object. By definition, a net drag in the flow results

in a negative efficiency from Eqs. (8) and (9) as the drag removes momentum and power from the flow. In the zero efficiency case (middle), the vortices are aligned to the centerline of the wake directly behind the propulsor. The vector addition from the vortices now results in motivation of the flow perpendicular to the direction of mean flow. The net change in the momentum of the fluid is zero. Any momentum gained by the fluid is negated by the opposing momentum of the fluid between the next two vortices. In this zero efficiency, zero momentum case the thrust force imparted by the foil is the same as the drag force imparted by the fluid on the foil. The positive efficiency case (bottom) is the opposite of the negative efficiency case. The vector addition from the vortices is being used productively to increase the momentum of the flow, which propels the foil through the fluid.

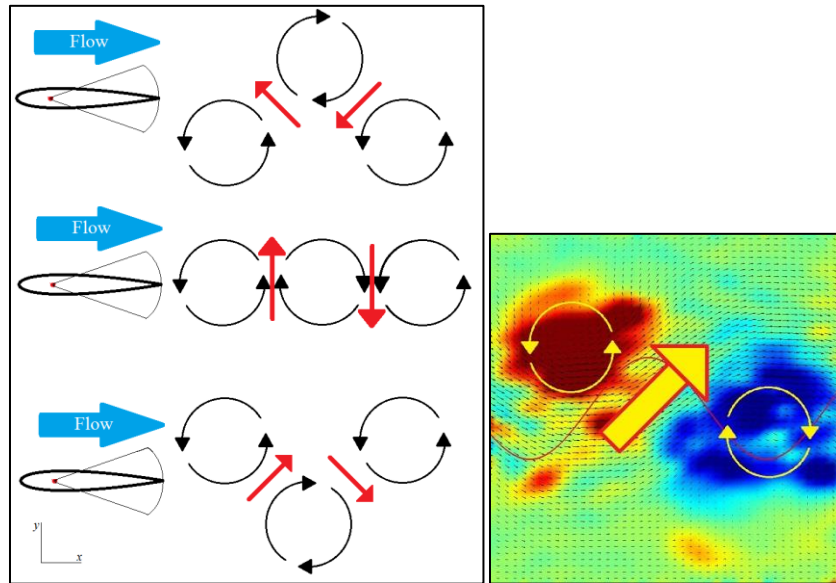


Figure 43: Expected wake vorticity interactions for a negative (top), zero (middle), and positive (bottom) efficiency case with an example from a maximum efficiency case of the Flex 60 foil.

The data intensive nature of PIV limits the number of runs where it can reasonably be used. Rather than testing the entire parameter space, PIV was used at selected points of interest determined after the load cell testing had covered the entire parameter space. Based on the load cell results for efficiency in Fig. 41, oscillations were selected for PIV analysis that would provide the broadest range of information about the hydrodynamic relationships while acquiring the least amount of data. Table 4 provides the three conditions that were selected from the rigid, Flex 60, and Flex 30 foils that represented the -50%, zero, and maximum efficiency points.

Table 4: PIV Parameter Space

Foil	Strouhal Number		
	-50% efficiency	Zero Efficiency	Maximum Efficiency
Rigid	0.15	0.23	0.55
Flex 60	0.18	0.33	0.56
Flex 30	0.21	0.42	0.62

For each oscillation, 25 angles were selected that would provide image capturing equally spaced in time. When the foil reached one of the 25 specified angles, the motor controller would trigger the PIV system to capture an image pair. Fifty image pairs were captured for each of the 25 angles in each of the nine runs of Table 4. Each set of 50 image pairs was preprocessed by subtracting out a mean image to increase the contrast of the illuminated particles in the flow.

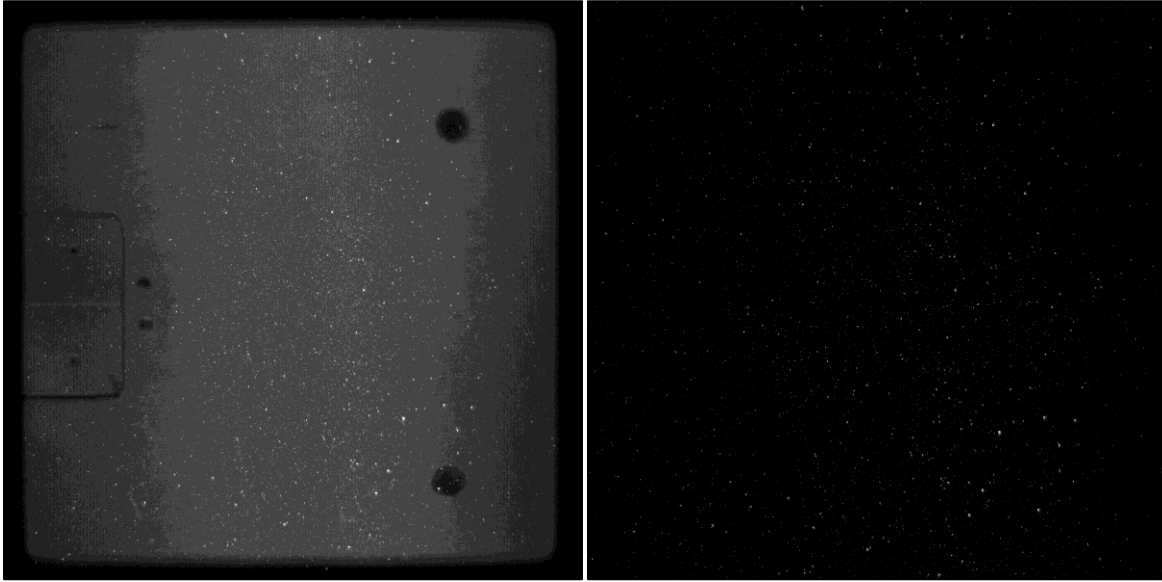


Figure 44: Image captured by the PIV system and the same image after preprocessing to remove the mean image.

Figure 44 shows one of the captured images alongside the same image after preprocessing. The total image frame covers an 11" x 11" square with 2084 pixels on each side; however, processing requires cropping the data near the edges, which results in a 9.84" x 9.84" square with 1824 pixels per side. This data range begins 1.88" behind the trailing edge of the propulsor, which is out of the images on the left side. The foils could not be included in because the reflected laser light would saturate the camera and reduce the contrast of the illuminated particles nearby in the flow.

After the images were preprocessed, the image pairs were processed one pair at a time using the OpenPIV image processing software (Taylor et al., 2010). The software performed the analysis using an interrogation window size of 32 pixels square equally spaced throughout the image with no overlap. With 1824 pixels available for processing in the image, a 57x57 vector field was generated for each image pair with a spatial resolution of 5.69 vectors per inch. The vector field was filtered using the OpenPIV software package to remove outliers and smooth the field. The 50 vector fields were then averaged into a single field that represented the velocity vector field for that angle in the oscillation. The curl of the velocity field was calculated to determine the 2D vorticity of any point in the frame captured by the PIV system. Generally, the curl of the vector field in three dimensions is calculated as the determinant of the matrix

$$\begin{bmatrix} \hat{i} & \hat{j} & \hat{k} \\ \frac{\partial}{\partial x} & \frac{\partial}{\partial y} & \frac{\partial}{\partial z} \\ u & v & w \end{bmatrix}, \quad (10)$$

where \hat{i} , \hat{j} , and \hat{k} correspond to the unit vectors in each of the three principle axes, and u , v , and w correspond to the velocities in those directions, respectively. For the two-dimensional case, there is no velocity in the \hat{k} direction and no differential in velocities moving up or down the z -axis. Thus, the determinant evaluates to

$$\left(\frac{\partial v}{\partial x} - \frac{\partial u}{\partial y} \right) \hat{k}. \quad (11)$$

The resulting vector is in the z direction either coming out of or going into the image depending on the rotation of the fluid at that point. The curl corresponds to the “right hand rule” where a counterclockwise vortex has a positive curl vector coming out of the page and a clockwise vortex has a negative curl vector going into the page.

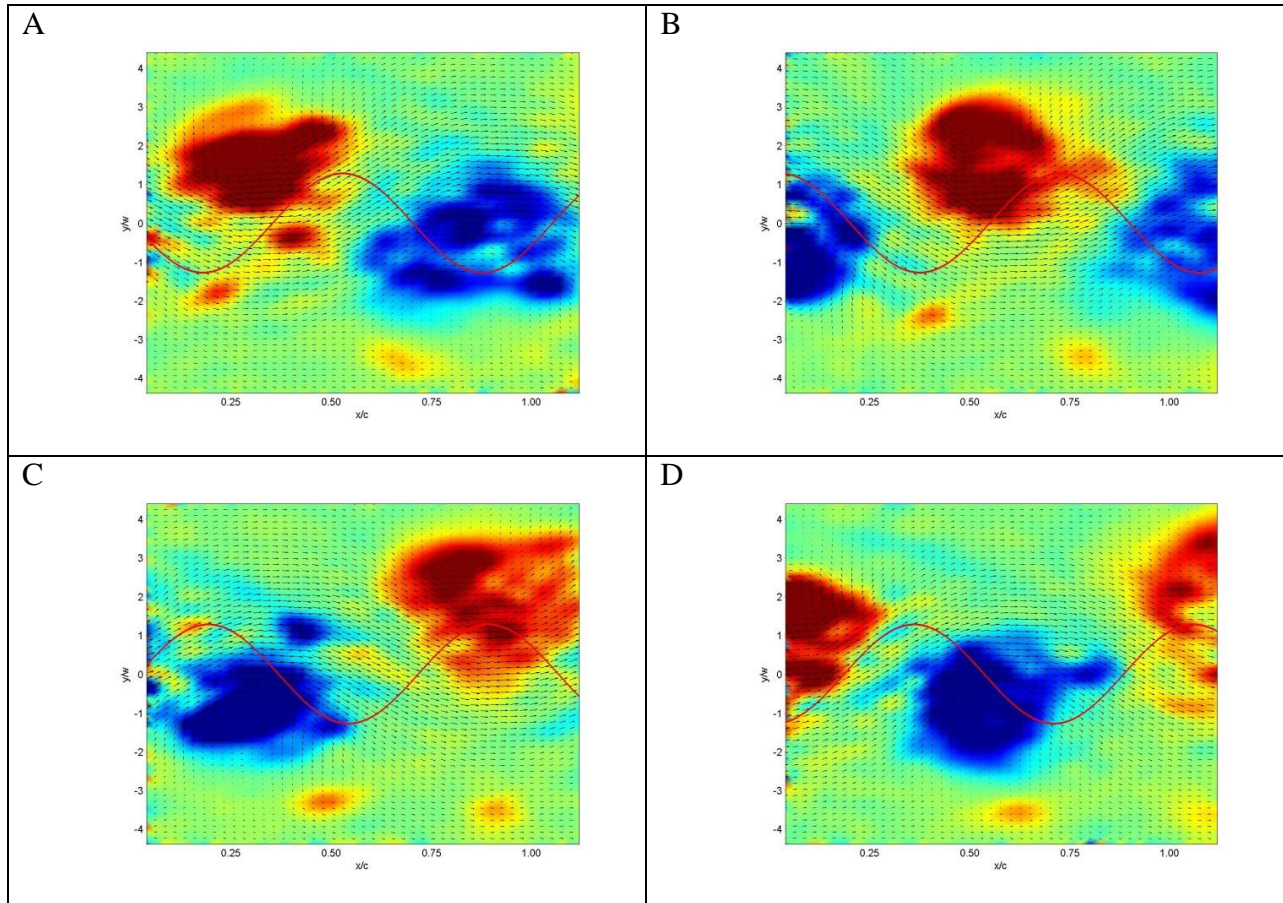


Figure 45: PIV images from each quarter cycle of the Flex 60 foil's maximum efficiency run (red = positive and blue = negative vorticity).

Figure 45 contains four PIV images from the high efficiency run of the Flex 60 foil. These images represent the vector field of the flow behind the foil. The tail of the foil is 1.88” out of view to the left of each of these images, and the flow is moving from left to right. The red areas

signify areas of positive vorticity (counterclockwise), and blue areas indicate negative vorticity (clockwise). The range of the colors was determined independently for each oscillation by two standard deviations from the mean to avoid outliers desaturating the data. The vectors on the image are representative of the phase-averaged velocity of the flow at that point. The sine wave represents the approximate position that the tail has travelled through the fluid, assuming the fluid is moving at the prescribed velocity for the run.

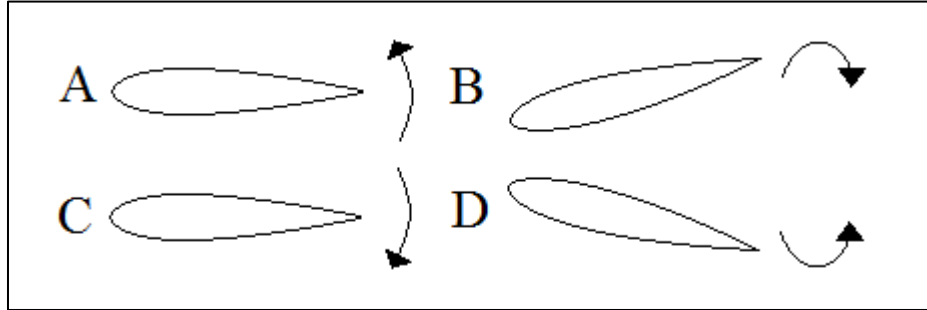


Figure 46: Image labeling convention used to reference foil location and direction of motion for all PIV images.

Figure 46 shows the convention for the image labels with regard to the foil position and direction of motion at the time each image was triggered. The “A” image represents the foil about to reach its zero angle position in the oscillation and moving in the positive (image: up) direction. The “B” image is a quarter cycle later as the foil reaches its most positive angle. The “C” image is the next quarter cycle when the foil is about to return to its zero position and is moving in the negative (image: down) direction. The “C” image is a near mirror image of the “A” image with opposite vorticity on opposite sides of the centerline. The “D” image is yet another quarter cycle later as the foil reaches its most negative angle. The “D” image is also a near mirror image of the “B” image.

The fluid velocity between any two vortices is larger than the free stream as the vortices motivate the flow in addition to its previous free-stream velocity. In the “A” image of Fig. 45, the positive primary vortex (red) has just been released from the foil after its creation when the foil was on its downward movement. The smaller auxiliary vortices are released slightly later than the primary vortex. The vorticity of the primary vortex is strong enough to pull in the nearest auxiliary vortex which eventually combines and assimilates into the main vortex in the “B” and “C” images, respectively. The farther auxiliary vortex, however, is not close enough to the main vortex to be pulled in. Rather, the positive angular velocity of the foil begins to form a negative primary vortex (blue) that pulls the farther auxiliary vortex into the slower moving flow outside of the wake where it lingers for another full oscillation cycle before leaving the image frame. Each of the primary vortices begins concentrated and just barely on its respective side of the centerline. As the vortices move downstream, they spread outward from the centerline and grow larger, but less concentrated, as they dissipate.

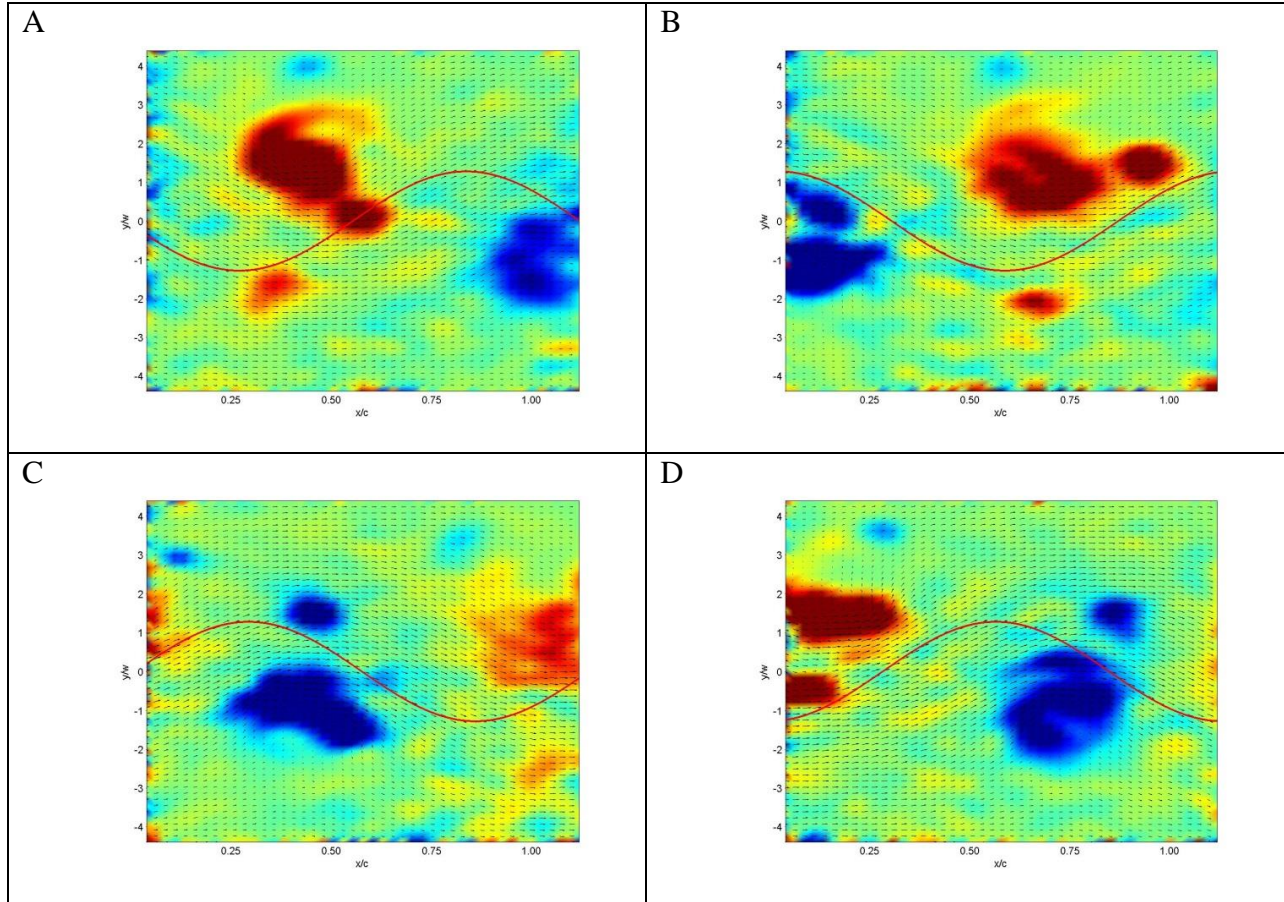


Figure 47: PIV images from each quarter cycle of the Flex 60 Foils zero efficiency run (red = positive and blue = negative vorticity).

Figure 47 shows equivalent images from the zero efficiency run for the Flex 60 foil. The sine wave indicating foil position has a longer wavelength due to the slower movement of the foil relative to the flow speed. In this run, the primary vortices are smaller and weaker than the ones formed in the maximum efficiency case. The auxiliary vortices, however, appear larger and stronger relative to the primary vortices. The stronger auxiliary vortices, rather than being quickly absorbed into the primary vortices, have enough energy to participate in a vortex dance with the primary vortex, where the two vortices spin around one another in the same direction as their vorticity. While this dance causes the first auxiliary vortex to move a considerable distance across the centerline, it pulls the primary vortex just slightly back towards the centerline. With both of the primary vortices closer to the centerline, their influence on and motivation of the flow continues deep into the wake. The second auxiliary vortex also shows similar behavior to the high efficiency case where it is influenced by the next incoming primary vortex of opposite vorticity.

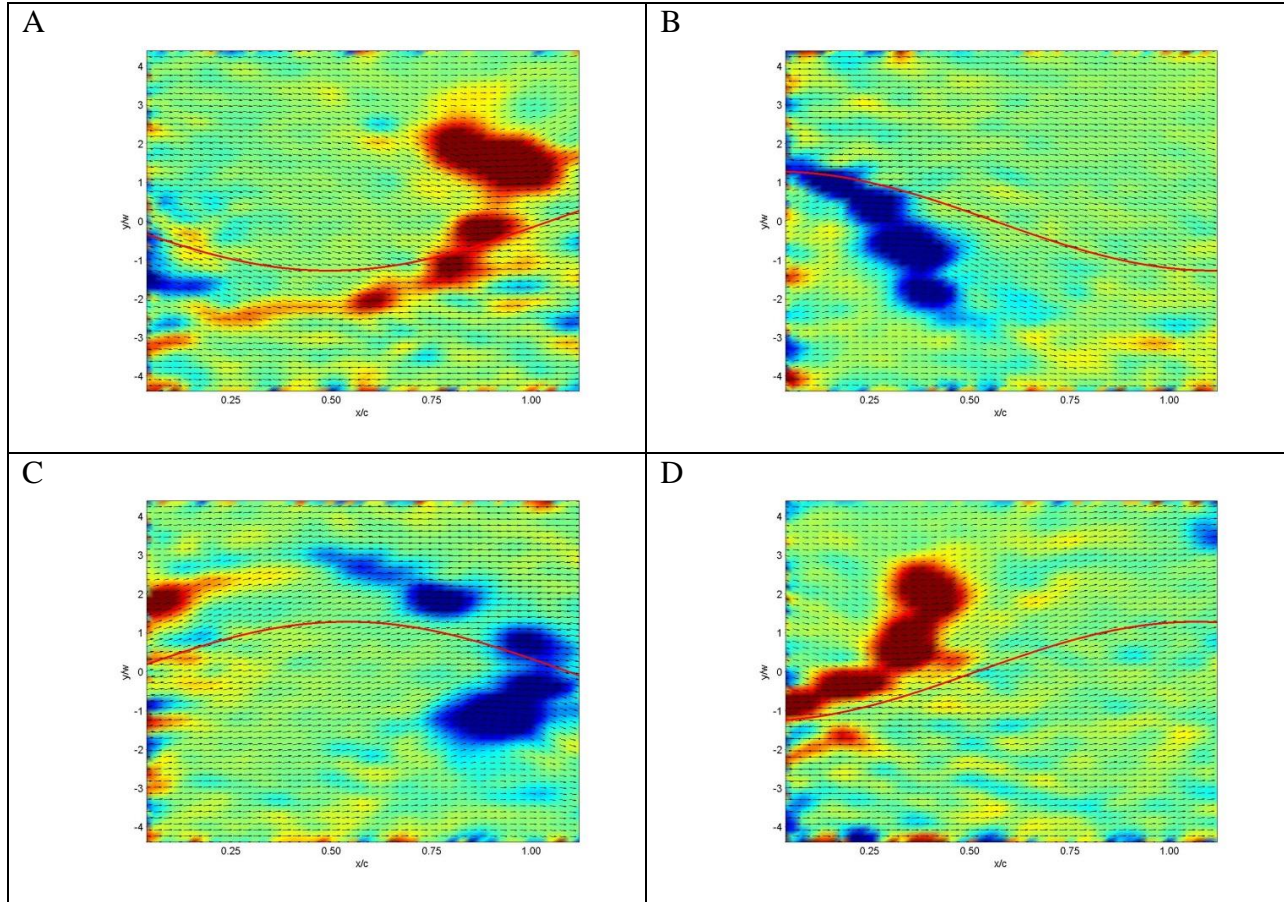


Figure 48: PIV images from each quarter cycle of the Flex 60 negative efficiency run (red = positive and blue = negative vorticity).

Figure 48 shows the negative efficiency PIV images for the Flex 60 foil. In this case, the movement of the foil is hardly enough to generate distinct vortices. The result is a long vortex train that begins as one long connected line but gradually coalesces into several discrete vortices. Because the foil is moving slowly relative to the velocity of the water, the distance increases between one vortex and the next, which decreases their collective interaction with the flow. There is only a slight disturbance in the velocity profile of the fluid between the vortices as the velocity vectors angle slightly in the direction of the constructive influence from the vortices.

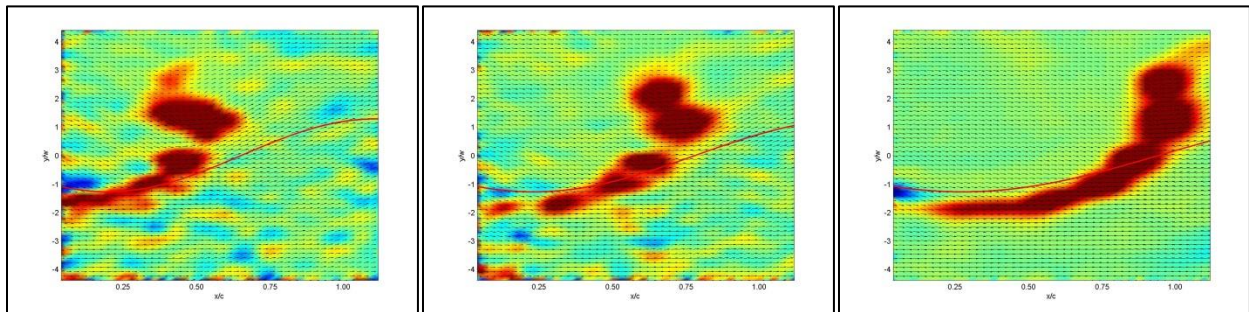


Figure 49: PIV images from negative efficiency run for Flex 30 (left), Flex 60 (center), and rigid (right) foils (red = positive and blue = negative vorticity).

Figure 49 shows a comparison of the vortices for the negative efficiency case of the Flex 30, Flex 60, and rigid foils. These images are from one eighth cycle after the “D” image shown in Fig. 47. All of the images display the same vortex train characteristic of a low Strouhal Number. The Flex 30 foil has the most coalescence of the vortex train, which generally indicates higher levels of vorticity. This result is partly due to the different oscillation parameters used to get the -50% efficiency for this set of images. Because the more flexible foils achieve the same efficiency at higher Strouhal Numbers, the Flex 30 foil is operating at a higher oscillation frequency relative to the speed of the surrounding fluid. The result is more vorticity in the water, which leads to the coalescence of the vortex train into discrete vortices. Also of note is the amount of noise present in the background of the images. While there appears to be almost no background noise in the rigid foil image, the noise increases for both the Flex 60 and Flex 30 foils. The same patterns were noted for the zero and maximum efficiency foil comparisons. While some of the noise may be a result of variances in capturing and processing the images, the amount of noise present suggests there is a relationship with the foil flexibility.

Also of note is the timing of the creation of the vortex. At the point these images were taken, the foil had returned from its most negative angular position by about 2.3° , and it had an positive angular velocity. For the rigid foil, the vortex train is fully detached from the foil, and the opposing vortex train is already being shed into the wake and into the image frame. For the Flex 60 foil, the full vortex train comes into view in the next $1/25$ cycle frame, but the opposing vortex does not begin to appear for another full eighth cycle as shown in the “A” image of Fig. 47. For the Flex 30 foil, the full train does not come into view for another two, $1/25$ cycle frames, and the opposing vortex train does not come into view for nearly a quarter cycle. The delay in vortex formation for the more flexible foils is likely a result of the geometric deformation of the foil during the oscillations. Because it is the trailing edge of the foil that ultimately sheds the vortices into the wake, its velocity and motion profile will have a significant effect on the timing of the vortex shedding. With the most rigid foil, there is effectively no lag between the angular position of the shaft and the tip, but as the foils flexibility increases, there is an increased lag in the tip position.

The flexible tip lag is especially significant at the maximum angular position. When the shaft reaches the maximum angular position and stops, the tip of the foil is still a small angle behind and still has a positive angular velocity. Before the foil tip reaches the maximum angle, however, the shaft moves in the opposite direction and begins accelerating the tip back in the opposite direction. The result is a swept distance that is less for more flexible foils. The flexible foils influence less water with every oscillation compared to the rigid foil, and the result is less thrust for the same oscillation parameters. A recent study suggests that there may be a resonant frequency of oscillation that would optimize the swept length of flexible propulsors for increased efficiency, but resonance was not taken into consideration for the experimental evaluation of the foils (Dewey et al., 2013).

The maximum efficiency case for the Flex 30 and rigid foils presents a unique case of a suspected pitchfork bifurcation due to the unstable dynamic system of successive alternating vortices staying relatively close to the centerline. Eventually the system stabilizes when the vortices flow in pairs away from the centerline, and all of the vortices remain on one particular side of the centerline.

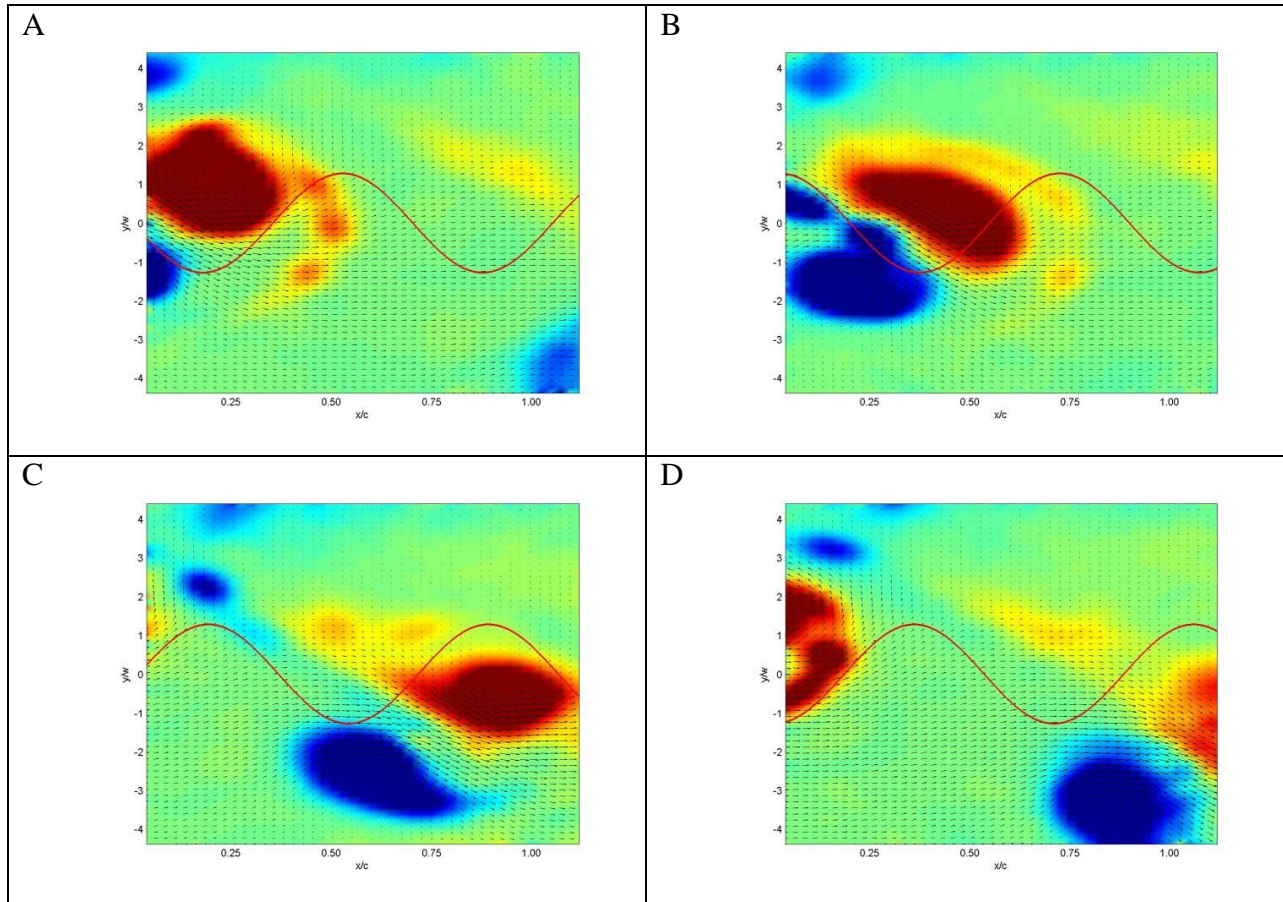


Figure 50: PIV images from each quarter cycle of the rigid foil's maximum efficiency case with negative pitchfork bifurcation (red = positive and blue = negative vorticity).

Figure 50 displays the high efficiency case for the rigid foil, in which there is a suspected pitchfork bifurcation in the negative direction. The “A” image shows the first primary vortex along with a few small auxiliary vortices that are beginning to orbit around the primary vortex. The primary vortex is fully detached and moving almost straight downstream at this point in the oscillation, but the formation of the opposing primary vortex causes the two vortices to begin walking downward as they propagate further into the wake in the “B” image. The walking vortex pair motivates more flow and higher flowspeeds on the bottom half of the image which pulls the vortices away from the trailing edge of the foil faster than if they were in a uniform velocity field along the centerline of the flow. In the “C” image, the formation of the third vortex is visible at the far left of the image, but the previous vortex pair is walking out of the range of influence of the newly forming vortex. If not for the bifurcation, the second primary vortex would be just in front of the newly forming third vortex and influence it upward and

farther away from the vortex forming in the “A” image. Because the vortex has walked out of the range of influence and the flow at the top half of the image is much slower, the third vortex slowly moves straight downstream, waits for the formation of a fourth vortex, and walks out of influence of the next set of vortices produced.

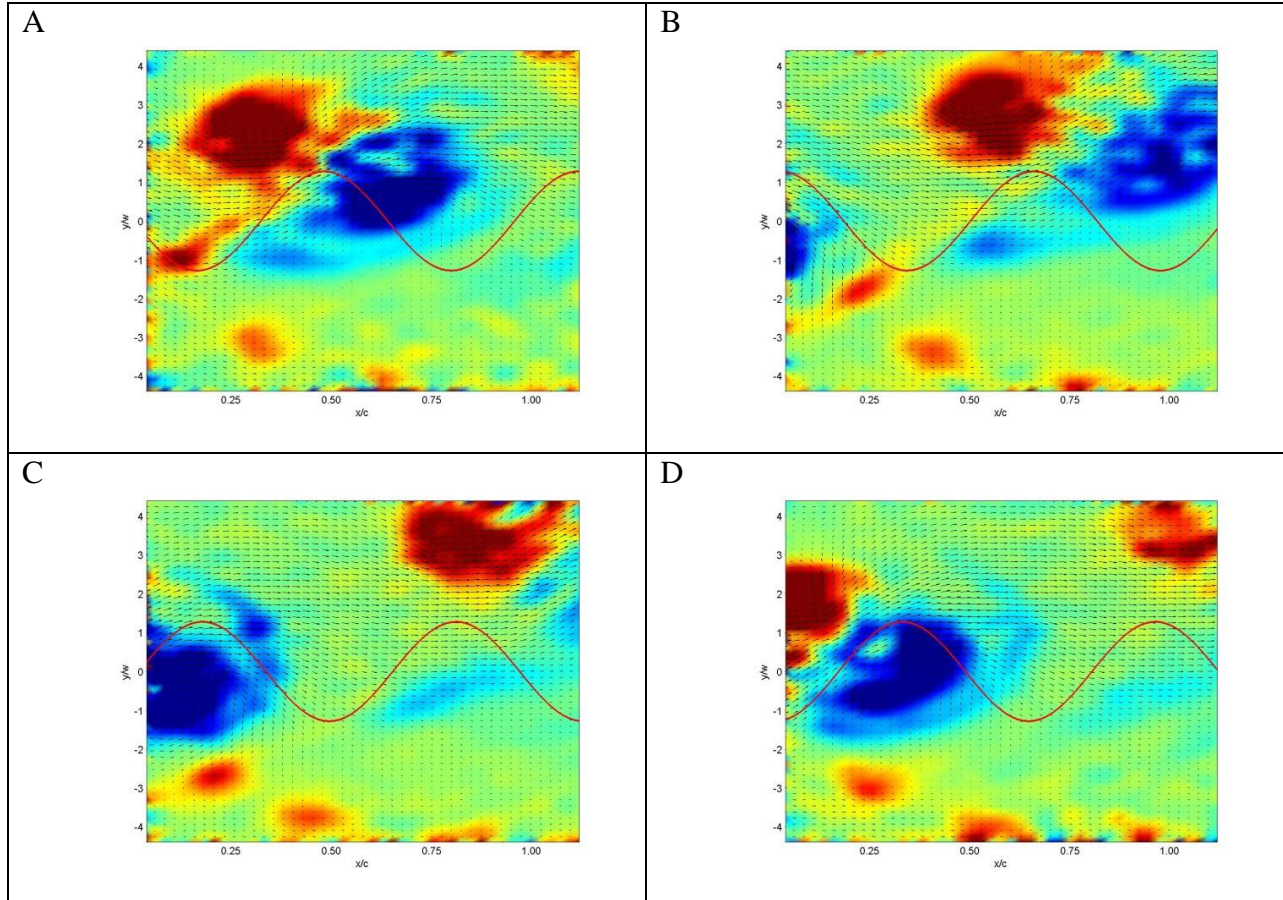


Figure 51: PIV images from each quarter cycle of the Flex 30 foil's maximum efficiency case with positive pitchfork bifurcation (red = positive and blue = negative vorticity).

Figure 51 displays a similar vortex wake asymmetry demonstrating positive direction behavior from the maximum efficiency case of the Flex 30 foil. This case is almost an exact opposite of that shown in Fig. 49, except that each of the images has a phase difference of about a quarter cycle due to the lag caused by the use of a flexible foil. Regardless of the delay, this case demonstrates that the bifurcation is possible in the opposite direction as well. The side that the vortices tend towards is likely due to slight variances in initial conditions that cause them to continuously tend towards one side for the remainder of the oscillation. Once the vortices begin to walk together in one direction, the system only further stabilizes and settles in a configuration displayed in the images above.

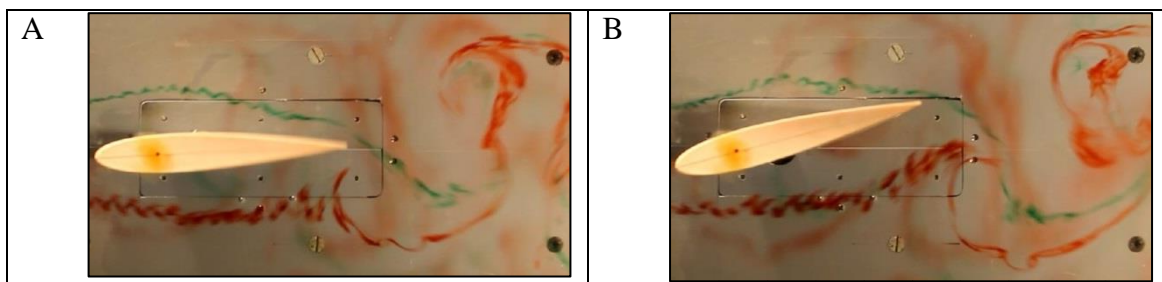
Dye Injection Analysis and Results

One disadvantage of the PIV measurement technique is that it cannot capture information about the flow adjacent to the foil. To gain additional information about the fluid-foil interaction next to and immediately behind the foil, a camera was placed underneath the test section while dye was injected into the flow, as shown in Fig. 52. To better discern the flow, pressurized green and red dye were injected on opposing sides of the foil. The dye was injected into the same mid-span of the foil where the PIV images were captured. The dye injection was only used for a few key locations in the parameter space as determined by the load cell and PIV results to supplement the results of both previous techniques.



Figure 52: Dye imaging of the Flex 40 foil during oscillations.

To provide a comparison to the PIV data, limited dye imaging was collected for runs involving high efficiency Strouhal Numbers for the Flex 40 and rigid foil. The dye imaging technique works best in slower, laminar flow patterns where the dye takes longer to disperse into the surrounding fluid. For the dye injection to be effective, only slower speed tests could be tested. The slower flow speeds correspond with higher Strouhal Numbers. Consequently, higher efficiency oscillations are easier to investigate with dye imaging because they usually occur at relatively high Strouhal Numbers.



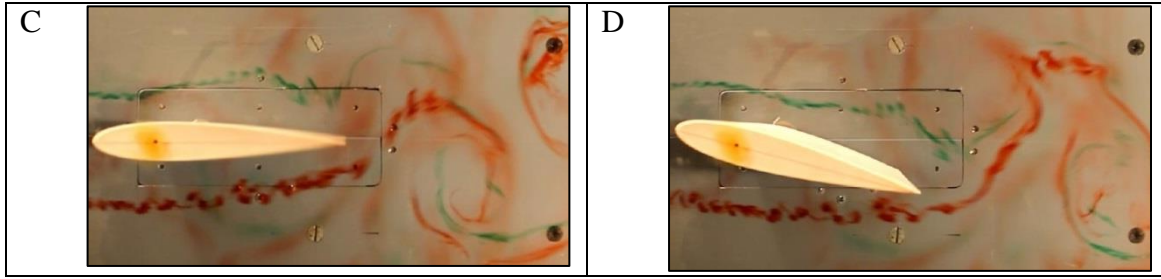


Figure 53: Dye injection images from quarter cycles of the high efficiency case of the Flex 40 foil.

Figure 53 shows the development of the vortices off the trailing edge of the Flex 40 foil in a high efficiency oscillation. In the “A” image, the foil is at its centerline and moving upward at maximum angular velocity. At this point, the red dye along the edge of the foil (image bottom) is being pulled towards the centerline by the void left by the foil and pushed downstream by the free-stream flow. The upward velocity of the flow is greatest at the trailing edge of the foil, but it quickly diminishes further in the wake. This gradient of perpendicular velocity in the streamwise direction creates vorticity, as defined by Eq. (10). In the “B” image, the foil is reaching its uppermost position and it has no angular velocity. The vorticity created in the previous image is now pulling in the green dye from the opposite side of the foil. Together with the vortex further in the wake, the vortices motivate a stream of fluid in the direction of the flow, which creates thrust for the foil. The “C” and “D” images show the opposing vortex forming at the trailing edge of the upper side of the foil.

Some additional fluid-foil interaction causes smaller vortex formation, visible in the bottom right corner of the “B” image as well as in the bottom right corner of Fig. 52. These smaller vortices are easily seen on both sides of the oscillation and are the result of a small amount of the flow being pulled backwards from the wake into the void left by the foil as it departs from its maximum angular position. The resulting gradient of the streamwise velocity perpendicular to the flow has both negative and positive values between the channel wall and the centerline. A small vortex with opposite vorticity of the large vortex is formed further away from the centerline than the primary vortex. These opposing vortices are also seen at the top of the PIV images in Fig. 47. The coupling of the small vortex and its nearby, opposing primary vortex causes a small amount of fluid to be motivated against the direction of flow. The opposing momentum decreases the power input into the fluid and results in slightly lower efficiencies. As the Strouhal Number increases, the free-stream flow decreases relative to the oscillation frequency, and the amount that flow in the wake would be pulled backward from the wake would likely increase and result in a stronger secondary vortex. A stronger vortex would remove more momentum from the flow and may be one of the contributing factors to the linearly decreasing efficiencies after the peak efficiency is reached. While the additional vortex is not likely the only cause of decreased efficiencies, mitigation of its formation through control of the motion profile and Strouhal Number of the propulsor on an underwater vehicle may improve performance.

Another disadvantage of the collection and processing technique used for the PIV is that it does not provide information about the formation of the vortices at the very beginning of the oscillation, starting with undisturbed free-stream flow. While study of this formation is not necessarily of interest for the ordinary, centerline vortex trajectories, the suspected case of the pitchfork bifurcation displays a unique case where the first formed vortices are equally spaced along the centerline, but later vortices are paired and off-center. Study of dye injection reveals information about the transition from a typical to the asymmetrical vortex configuration.

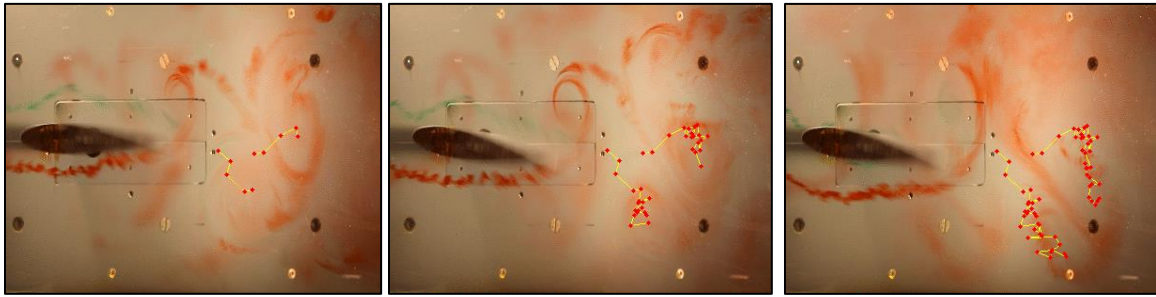


Figure 54: Tracking of the vortex location for the suspected case of the pitchfork bifurcation for the maximum efficiency case of the rigid foil.

Figure 54 shows the approximate positions of the vortices tracked from the first oscillation of the foil until there is a fully developed asymmetry in the vortex shedding pattern resulting in paired vortices moving together towards the bottom of the image frame. Each red dot represents the approximate position of the vortices for each successive oscillation cycle. The length of the yellow line between the dots represents the amount that each vortex has moved since the previous oscillation cycle. The left image of Fig. 54 shows that the first vortices initially formed on the centerline of the wake, but they quickly moved to their respective sides of the centerline. In the middle image, the vortices have mostly stayed on opposing sides of the centerline, but they have begun to slowly creep downward in the image. The final image in Fig. 54 shows the fully developed positions of the vortex pair at the bottom right corner of the image frame. This image closely resembles the PIV images from Fig. 50. At no point in time does there ever appear to be any vortex formation in advance of the foil that contributes to the asymmetrical vortex propagation in the wake.

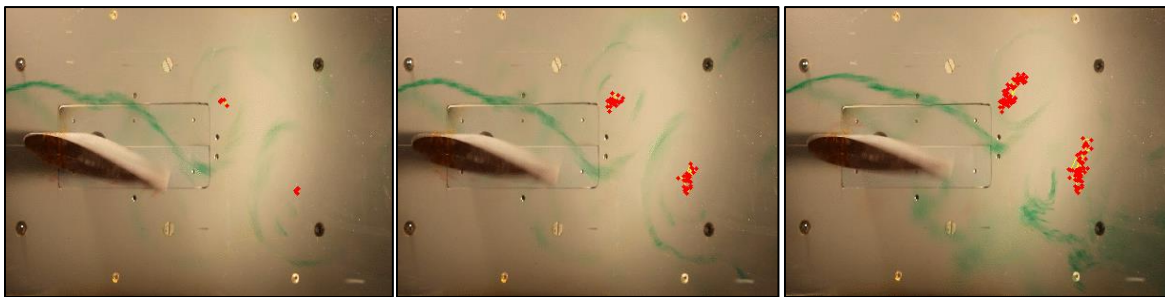


Figure 55: Tracking of the vortex location for the suspected case of the pitchfork bifurcation in the opposite direction for the maximum efficiency case of the rigid foil.

Although the majority of the dye injection images captured for the high efficiency case of the rigid foil were nearly identical to the image sequence in Fig. 54, one exception was captured in Fig. 55 that found the paired vortices favoring the opposite side of the channel. Unfortunately, the images were captured when the red dye reservoir had run out of dye. The situation occurred within the same captured video as another run where the vortices favored the same side as in Fig. 54. During the video, the motor briefly stops in the center position as it comes to the end of one of its programmed oscillations and immediately begins another oscillation at the same frequency. The total time between the two oscillations is less than five seconds, but it is long enough so the vortices flow downstream, and shedding mode resets. When the new oscillation begins, the vortices start in their same initial positions on opposite sides of the centerline, as shown in the left image of Fig. 55. Rather than the vortices pairing and moving downwards in the image, they remain stable on opposite sides of the centerline, and slowly begin to move upwards in the center image. The vortices finally reach a flow case where they pair and move towards the top of the image frame in almost the exact opposite manner as in Fig. 54.

The opposite nature of this vortex pairing lends credence to the possibility of the flow case being classified as a pitchfork bifurcation. There is no visible difference in the motor oscillation or initial flow conditions. The cause of the preferred side of the vortices could be something as minor as minute variances in the velocity profile of the flow, fluctuations in power to the motor, or slight computing delays within the motor controller. The number of cycles that passed before the vortices paired in Fig. 55, however, suggests that some parameter of the maximum efficiency, rigid foil oscillation causes the vortices to preferentially pair in the more common orientation seen in Fig. 54. Further investigation of the suspected bifurcation may allow the parameters to be adjusted such that the preferred vortex shedding side could be controlled. This could allow shallow, submerged vehicles to control their wake and limit the amount of vortex interaction with the surface to help prevent detection.

Conclusions

Although the majority of previous research indicated that a flexible foil should see increased performance over its rigid counterparts, the hypothesis proved to be incorrect for the parameter space used in the testing. One possible explanation for the discrepancy is the flow speeds at which the experiments were run. On average, the flow speeds for this experiment were an order of magnitude greater than the speeds of previous research, but they were more representative of what would be seen by an actual marine propulsor. The discrepancy makes it likely that the efficiency of a flexible propulsor depends not only on the Strouhal Number and Stiffness Constant, but also on another parameter such as the Reynolds Number, reduced resonant frequency, or some other dimensionless constant.

The general trends of thrust and efficiency measured in the experimental assessment of the foil match those of numerical models. The comparison between the rigid foil efficiencies increases the confidence in the results from both the numerical model as well as the experimental setup,

but there are still some unaccounted discrepancies between the model and experimental data for the rigid foil. For the flexible foils, the predicted trends of increased efficiency in the numerical model were the opposite of the trends noted by the load cell data. This suggests that there are significant parameters of the flexible propulsor's interaction with the fluid that are not taken into account in current numerical models.

The collection of load cell data with the three-dimensional plot between Strouhal Number, Stiffness Constant, and efficiency helps to quantify the unique relationship between the three parameters. Defining this relationship provides a framework to estimate the performance of flexible propulsors for similar applications in the future. However, the discrepancy in the trends of efficiency between the various Stiffness Constants must be resolved before flexible propulsor technology can be productively applied.

The PIV data reveal additional information about the relationship between the flexibility of the foils, the oscillation parameters, and the resulting performance through analysis of the vortices in the wake. The data explain and confirm the results from the load cell analysis by providing insight into the physical differences in the vortex interactions in the wake of the propulsors. Matching the calculated efficiency to various vorticity trends in the wake reveals a more complex causation for negative efficiencies than merely the orientation and position of the vortices in the wake. Rather than the von Kármán vortex produced by flow over passive bodies, the majority of the vortices are shed in long, sometimes continuous, trains for the negative efficiencies as opposed to the large, discrete vortices shed by the high efficiency cases. This vorticity indicates that the foil is not just passively producing drag, but the motion of the oscillation is actively contributing to the negative efficiency.

The PIV data additionally show narrower vortex shedding for the more flexible foils, which suggests the trailing edge of the flexible propulsor is not reaching a full $\pm 15^\circ$ during oscillations due to its flexibility. The more flexible foils thus have a shorter swept length during the oscillations. Because the swept length is in the numerator of the Strouhal Number in Eq. (2), flexible foils would have lower Strouhal Numbers. Accounting for this fact through measurement of the propulsor deformation and swept length in each run may increase the correlation of the efficiency in terms of the locations of the zero and maximum efficiency, but the peak efficiency seen by the flexible foils would remain less than for the rigid foil.

The dye imaging further explained some of the questions that arose from the correlated PIV and load cell data. The dye revealed in more precise detail how the vortices are shed from the tail of the propulsor and explained the source of some of the additional vorticity in the wake of the foil that may have otherwise been ignored or treated as noise in the PIV analysis. The suspected case of the pitchfork bifurcation was also investigated more thoroughly through the dye injection in order to follow the development of the asymmetry and demonstrate the double-sided nature of the phenomena.

Future Work

Investigation of the properties of propulsor technology is a continuing process in order to emulate biological swimming techniques for underwater vehicles. Although the flexible propulsors did not perform as well as expected in the experimental assessment of the foils, not enough is known about their properties to completely rule them out as a viable option for marine propulsion. The following areas are recommended for future investigations for the possible application of the pitching flexible propulsor.

By proportionally reducing the flow speed and oscillation frequency of each run, the same Strouhal Numbers may be tested at other Reynolds Numbers and Stiffness Constants. This testing would investigate the involvement of those parameters in the overall performance of the flexible propulsor. The conduct of this testing, however, would require a smaller rated motor and load cell with increased resolution for performing low frequency runs and accurately measuring smaller forces. Altering foil geometry such as the chord length, NACA designator, or axis of rotation may also provide better flexible foil performance in future tests.

Other oscillation profiles as opposed to the $\pm 15^\circ$ sine wave used may also provide better performance. The PilotFish project demonstrated in 1997 that large, single rotations of flexible propulsors allows for significant force production. These large forces can provide quick acceleration and deceleration for underwater vehicles. The flexible foils may provide improved performance compared to rigid foils in these kinds of motions.

Consideration of a reduced resonant frequency, the ratio of oscillation frequency to resonant frequency, may allow for proper tuning of flexible oscillation parameters for increased performance. Operating at or near a resonant frequency may increase the swept length of the flexible propulsors and allow them to influence a higher percentage of the flow in the channel. Finding the resonant frequencies for the flexible propulsors would require high-speed imaging that could capture the instantaneous shape of the foil for any given oscillation.

Further investigation into the bifurcated flow case may also provide insight into the fluid-foil interaction and reveal the most significant viscous mechanisms during the oscillations. Quantifying these mechanisms would allow numerical models to be updated with new parameters that take into account viscous effects. The bifurcation may also be able to be controlled or artificially stabilized by altering the foil oscillation slightly.

Because the project was experimental in nature, closer comparison to panel code, including simulation of the exact cases from the experimental assessment, may provide additional insight into the underlying physical phenomena. Because the current panel code is unable to account for viscous boundary layer dynamics, more complex vortex shedding patterns, stall from flow separation, and pressure and form drag, comparison of the experimental and numerical results should reveal specific details about the extent that each of those factors affects the fluid-foil interaction. The amount of variance between the panel code and the experimental results will

indicate the contribution of each of those factors to the overall performance, and allow the panel code to be updated to consider those factors, if necessary.

Additional PIV analysis of the parallel horizontal planes in the wake of the propulsor may help determine the extent to which the 2D flow assumption is valid. While the turbulent flow will inherently have a three-dimensional velocity field, the 2D assumption of a full span model means that the local flow statistics do not depend on the spanwise position along the foil. Investigation of the foil in a 3D flow condition may suggest what span lengths are necessary in order to consider the 2D assumption valid for application.

Further investigation with dye imaging and PIV of auxiliary vortices possibly shed at higher Strouhal Numbers may provide additional details about the causes of various vortex shedding modes for the flexible propulsor. From the analysis, the vortex shedding patterns that reveal the highest efficiencies from the most motivation of flow in the streamwise direction can be emulated in applications to marine systems.

Research Contributions

Through the experimental testing of the pitching flexible propulsor, this project provides data that may contribute to an update of current theory regarding the hydrodynamic interaction between the foil and surrounding fluid. Specifically, the project quantifies the performance characteristics of the pitching flexible propulsor within a parameter space applicable to the engineering of marine propulsors. The data will help future engineers determine if this technology is suitable for various marine propulsion applications. The flexible propulsor could potentially have applications that alter the Naval and Commercial Fleets of tomorrow. Naval Submersible Ships could especially benefit from this technology to provide greater maneuverability. It could also be the future for smaller AUVs that might require the ability to orient themselves correctly in tight quarters for reconnaissance, hull inspections, or in-port security. For surface ships, flexible propulsors could provide increased maneuverability at low speeds and reduce the need for tugs and the auxiliary propulsion units currently found on U.S. Frigates. The lack of a need for wash over a rudder could make the stressful situation of in-port maneuvering into a task no more difficult than parking a car on an empty street.

References

- ASTM Standard D412 (2013). Standard Test Methods for Vulcanized Rubber and Thermoplastic Elastomers – Tension. ASTM International. West Conshohocken, PA.
- ASTM Standard D638 (2010). Standard Test Method for Tensile Properties of Plastics. ASTM International. West Conshohocken, PA.
- Dia, H., H. Luo, P.J.S.A. Ferreira de Sousa, and J.F. Doyle (2012). Thrust performance of a flexible low-aspect-ratio pitching plate. *Physics of Fluids*, **24**, 101903.
- Dewey, P.A., B.M. Boschitsch, K.W. Moored, H.A. Stone, and A.J. Smits (2013). Scaling laws for the thrust production of flexible pitching panels. *Journal of Fluid Mechanics*, **732**, 29-46.
- Mueller, T. (2008). Biomimetics, Design by Nature. *National Geographic*, **213**, 4.
- Murray, M.M. (1999) Hydroelasticity Modeling of Flexible Propulsors. Ph.D. Dissertation, Duke University, Durham, NC.
- Murray, M.M., and L.E. Howle (2003). Spring stiffness influence on an oscillating propulsor. *Journal of Fluids and Structures*, **17**, 915-926.
- Rohr, J.J. and F.E. Fish (2004). Strouhal numbers and optimization of swimming by odontocete cetaceans. *The Journal of Experimental Biology*, **207**, 1633-1642.
- Schnipper, T., A. Andersen, and T. Bohr (2009). Vortex wakes of a flapping foil. *Journal of Fluid Mechanics*, **633**, 441-423.
- Taylor, Z.J., R. Gurka, G.A. Kopp, A. Liberzon (2010). Long-Duration Time-Resolved PIV to Study Unsteady Aerodynamics. *Instrument and Measurement, IEEE Transactions*, **59**, 12, 3262-3269.
- Triantafyllou, M.S., A.H. Techet, and F.S. Hover (2004). Review of Experimental Work in Biomimetic Foils. *IEEE Journal of Oceanic Engineering*, **29**, 3, 585-594.